A Computational Examination of Side-by-Side Rotors in Ground Effect




Richard Healy* *Ph.D. Student*
Joseph McCauley *Masters Student*
Farhan Gandhi *Redfern Professor*
Onkar Sahni *Associate Professor*
Center for Mobility with Vertical Lift (MOVE), Rensselaer Polytechnic Institute, Troy, NY

This study investigates the interactional aerodynamics of hovering side-by-side rotors in ground effect. The 5.5-ft diameter, three-bladed fixed-pitched rotors are simulated using computational fluid dynamics at a targeted 5 lb/ft^2 disk loading. Simulations are performed using the commercial Navier–Stokes solver, AcuSolve®, with a delayed detached eddy simulation model. Side-by-side rotors are simulated at two heights above the ground ($H/D = 0.5$ and $H/D = 1$), and with two hub–hub separation distances ($3R$ and $2.5R$). The performance of side-by-side rotors in ground effect (IGE) is compared to isolated rotors out of ground effect. Between the side-by-side rotors IGE, a highly turbulent mixing region is identified where the wakes of each rotor collide. The flow fountains upwards, as well as exits outwards (along a direction normal to a plane connecting the two rotor hubs) with fountaining between the rotors reaching up to 0.75D above the ground. As blades at $H/D = 0.5$ traverse the highly turbulent flow, strong vibratory loading is induced and a thrust loss is observed over the outboard sections between the rotors that is large enough to negate any nominal ground effect benefits inboard. Side-by-side rotors at $H/D = 0.5$ with $2.5R$ hub–hub spacing produce peak-to-peak thrust oscillations up to 16% of the steady thrust. Rotors placed higher, at $H/D = 1$ are positioned above the turbulent mixing flow and produce significantly lower vibratory loads. The spacing between rotors at $H/D = 0.5$ and $3R$ hub–hub separation allows strong vortical structures to develop between the rotors which move from side to side over multiple revolutions. When the vorticity moves closer to one of the rotors, it produces a greater lift deficit over the outboard region and a stronger vibratory loading. For rotors closer together, at $H/D = 0.5$ and $2.5R$ separation, the vortical structures between rotors are constrained to a more concentrated area and show less side-to-side drift.

Introduction

Over the last few years, there has been a significant interest in large multirotor eVTOL aircraft for urban air mobility. One of the challenges associated with the modeling, simulation, and performance prediction of these aircraft is the complex interactional aerodynamic flow fields of multiple rotors operating in close proximity. Several recent studies have used high-fidelity computations to represent these flows (see for, e.g., Refs. [1–8]), resulting in valuable physical insights as well as an understanding of beneficial geometries/configurations. It should be noted, though, that the above multirotor eVTOL interactional aerodynamic studies have all been conducted out of ground effect (OGE). During takeoff and landing operations, however, these multicopters will be close to the ground, and rotor–rotor–ground aerodynamic interactions can be expected to strongly influence the performance and loads.

Although the understanding of rotors IGE is not new, the majority of prior studies in this area have focused on conventional single main rotor aircraft or an isolated rotor in proximity of the ground. Early experiments by Fradenburgh (Ref. [9]) identified performance improvements for rotors operating near the ground and characterized how the wake moves radially outward after impacting the ground. Fradenburgh also identified flow inside the rotor wake moving upwards, towards the rotor disk. Other experiments have consistently reported improved rotor performance when operating within one rotor diameter of the ground and have been used to develop empirical models for rotors IGE (Refs. [10–13]). Experimental studies of rotors in forward flight ground effect have also revealed flow recirculation at low advance ratios leading to unsteadiness and an increase in power (Refs. [14–17]).

In recent studies, combinations of computational and experimental methods have been used to further understand ground effect aerodynamics. Several works have used free-vortex wake models to predict the radial wake spread of hovering rotors IGE as well as the recirculating flow of forward-flight rotors IGE (Refs. [18–22]). Experiments and computational fluid dynamics (CFD) simulations by Wadcock et al. also observed significant flow unsteadiness and upwash through the middle of the rotor disk due to ground effect on a UH-60 (Ref. [23]). Similar findings have been reported by Kutz et al. who observed a 21% increase in thrust as well as load oscillations when a Hughes 300C was simulated near the ground using CFD (Ref. [24]). Fluctuations in power have also

*Corresponding author; email: healyr@rpi.edu.
Revised version of paper presented at the 77th Annual Forum of the Vertical Flight Society, Virtual, May 10–14, 2021. Manuscript received September 2021; accepted December 2022.

been reported by Brown and Whitehouse who describe unsteadiness due to flow fountaining through the hub region in hover, as well as flow being reingested into the rotor during low-speed forward flight [25]. At smaller scales, Lakshminarayan et al. simulated a microscale rotor IGE and observed a thrust increase given constant power relative to when operating OGE (Ref. [26]). Flow unsteadiness was also observed below the rotor, which grew stronger as the rotor was brought closer to the ground.

While much of the existing literature on ground effect is for single main rotor helicopters, there exists a body of work providing insights specific to CH-47 tandem rotors IGE (Refs. [27–29]) as well as V-22 and XV-15 tilt rotors (Refs. [30–33]). The focus of tandem rotor configurations has mostly been related to the impact of rotor overlap on outwash; however, most large eVTOL vehicles employ nonoverlapped rotors for thrust generation and control. Tiltrotors in hover provide more relevant insights into multirotor operation IGE with ground effect-like conditions being observed on portions of the rotor disks positioned over the wings. Rotor outwash over the wings has been shown to fountain up, over the centerline of the vehicle and be reingested into the rotors, leading to reduced rotor performance (Refs. [30–33]). The unique aerodynamics of these multiple close proximity rotors has prompted investigations into other multirotor configurations of IGE. Actuator disk CFD simulations on a quad-tiltrotor by Gupta and Baeder showed highly complex flows between rotors when in close proximity to a ground plane (Ref. [34]). Other experiments on a quad-tiltrotor by Radhakrishnan and Schmitz attributed performance improvements IGE to upwash induced by colliding rotor wakes impinging on the underside of the fuselage (Refs. [35–38]). Multirotor interactions IGE have also been reported by Miesner et al. who simulated the 18 rotor Volocopter 2x using CFD and saw load fluctuations strengthen as rotors were brought closer to the ground (Ref. [39]). Fluctuations were linked to mixing vortex structures between rotors which grew stronger close to the ground. Larger vortex structures were observed between rotors that were spaced farther apart.

The present work uses high-fidelity blade-resolved CFD to further investigate the aerodynamics of multiple close proximity rotors IGE. In particular, comparisons are made between single rotors and side-by-side rotors operating near the ground. Rotor-to-rotor spacing and height above the ground are varied, and the aerodynamic interaction between rotors and the ground is investigated. Physical explanations for differences in rotor performance between cases are also provided.

Analysis

Three single rotor and four side-by-side rotor cases are simulated using CFD. Single rotors are simulated in hover OGE, at 0.5 rotor diameters above the ground (H/D = 0.5), and at 1 rotor diameter above the ground (H/D = 1) as shown in Fig. 1. Side-by-side rotors are also simulated in hover IGE at H/D = 0.5 and H/D = 1, for two hub-to-hub separation values: 2.5*R* and 3*R* (also shown in Fig. 1). For the two rotor cases, the left rotor spins clockwise and the right spins counterclockwise.

The rotors used have a 5.5-ft diameter, with specifications detailed in Table 1, and are fitted with an idealized teardrop-shaped hub to reduce (albeit not eliminate) the root wake and upwelling through the hub (Refs. [40,41]). The Rensselaer Multirotor Analysis Code (RMAC) (Ref. [42]), based on blade element theory (BET) with 3×4 finite state Peters–He inflow representation is used to evaluate an appropriate root pitch and RPM for a target 5 lb/ft^2 disk loading in hover OGE. A 22° root pitch and a rotational speed of 1600 revolutions per minute are found to provide low power and hover tip Mach number. A low tip Mach number is desired to avoid compressibility effects and reduce noise. Rotor RPM is held constant for all cases while comparing rotor thrust and torque in different configurations and conditions.

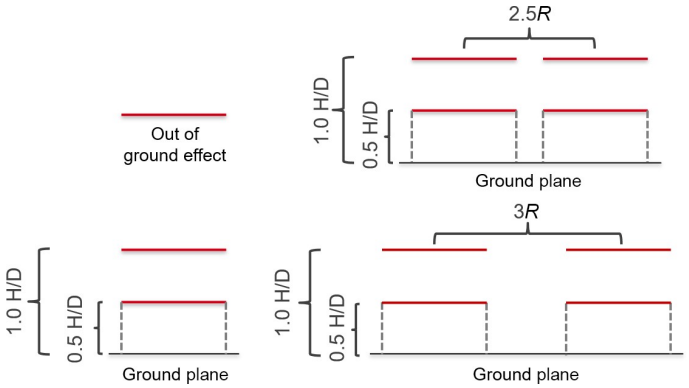

Fig. 1. Simulation cases: three single rotors and four side by side.

Table 1. Rotor parameters

Parameter	Specification
Diameter	5.5 ft
Number of blades	3
Solidity	0.076
Root cutout	0.2*R*
Airfoil	NACA 23012
Twist	−10°/span
Planform	Rectangular
Chord	3.28 in
Root pitch	22°
RPM	1600 rpm

All simulations are conducted using the commercial Navier–Stokes solver AcuSolve®, which uses a stabilized second-order upwind finite element method and is validated for external aerodynamic flows (Refs. [43, 44]). AcuSolve® simulation results for an SUI Endurance rotor in hover were previously shown to compare well against experiment in Ref. [1] where thrust at two different rotor speeds in hover matched experiment within 3%. Power predictions for the same rotor lie within 10% of that predicted by OVERFLOW (Ref. [45]), though these OVERFLOW simulations do not have power validation with experiment as experimental power included motor losses. In addition to this OGE hover validation, AcuSolve® simulation of an IGE rotor has also been compared to experiment reported in Ref. [10]. The IGE thrust predicted by AcuSolve® is found to differ from experiment by 0.85%, with additional details presented in the Appendix. For a two-rotor unit, the computational domain is shown in Fig. 2. The nonrotating volume is a rectangular prism with sides at least 25 rotor radii away from the front rotor hub. The sides and top boundaries are set to outflow with backflow conditions enabled, which allows for flow in either direction across the boundary with zero pressure offset. The bottom surface is set to no-slip condition in a weak fashion with a log-law based wall function (Ref. [46]). The weak boundary condition acts like a wall model (Ref. [47]) without the impractical computational cost associated with resolving the boundary layer on the ground. No-slip wall condition (enforced strongly or weakly) has been found to capture viscous effects which are associated with predicting rotor performance IGE (Ref. [48]). Around each rotor is a cylindrical rotating volume with radius 1.06 rotor radii and extending two chord lengths above and below the extents of the rotor hub. Each surface of the cylindrical rotating volumes has a sliding mesh interface which passes information to and from the nonrotating volume that comprises the remainder of the computational domain.

The computational domain is discretized using an entirely unstructured mesh comprised of tetrahedral elements. On each blade, the surface

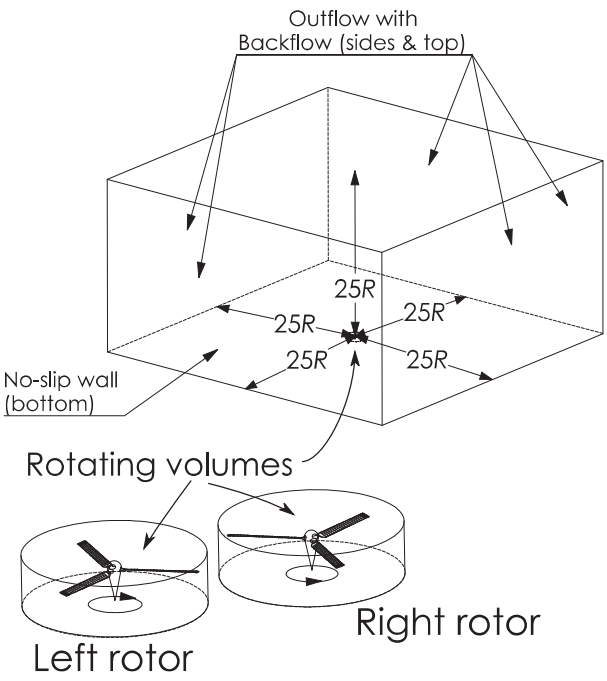

Fig. 2. Diagram of the computational domain.

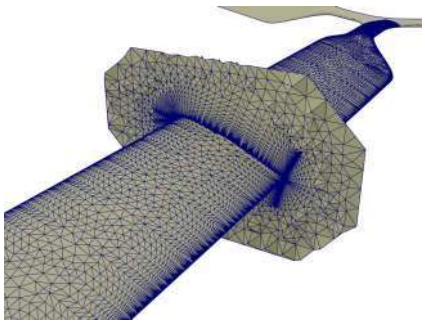

Fig. 3. Blade surface mesh viewed near midspan and a chordwise slice showing the boundary layer mesh in the wall-normal direction.

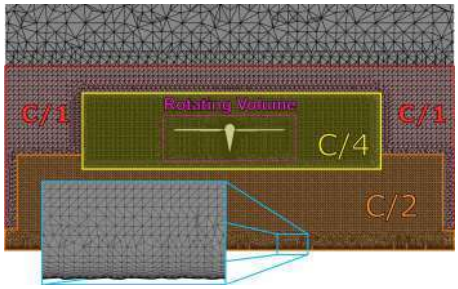

Fig. 4. Cross section of wake mesh refinement.

mesh is set to ensure 200 elements along the blade span and 200 elements around the airfoil contour, with refinement along the leading and trailing edges (0.14% chord first element height and 1.125 growth rate). The boundary layer in the wall-normal direction is highly resolved, with the first element height set to ensure a $\Delta y+ < 1$, which conforms to the requirements in Ref. [49] and is consistent with those used in Ref. [50]. The boundary layer is grown until the last layer size is within 80% of the local off-body element size (43 layers total). A portion of the blade surface mesh and a clipped slice of the boundary layer mesh is shown in Fig. 3. Around the rotors (0.75R above and below), a cylindrical wake refinement region (2.5R radius) is defined in which the element size is prescribed as 0.25 blade chord (shown for a single rotor in Fig. 4). Below the first refinement region is a second refinement region which is prescribed with elements 0.5 blade chord in size (Fig. 4). This refinement region extends radially from each rotor hub, extending 1.5R above the ground with 3.5R radius, and 0.5R above the ground with 10R radius. A third refinement region with 1.0 blade chord element size extends radially 10 rotor radii from each rotor hub and 3.25R above the ground (Fig. 4). A boundary layer mesh is grown off of the ground to capture the associated viscous effects. For this boundary layer, ensuring a $y+ < 1$ across the entire ground plane incurs substantial computational cost that can be avoided in this case through the use of wall modeling, which allows for $y+ < 100$ to be acceptable. At this grid scale, weakly enforcing no-slip conditions with log-law based wall models has been shown to capture the same mean-flow quantities as those produced by a fully resolved boundary layer (Ref. [47]). The use of wall modeling on the ground plane is estimated to save approximately 25 million elements for each isolated IGE case and 32 million elements for each side-by-side IGE case. For side-by-side rotor cases, a box-shaped refinement region is prescribed between the rotors with elements 0.25 blade chord in size. The box extends 0.75R in both directions laterally, 2R in both directions longitudinally and 2R in both directions vertically from the center point between both rotor hubs. Based on the results in the Appendix, this degree of interrotor refinement is deemed to be sufficient, with integrated thrust and torque changing by less than 1.0% compared to a mesh with 0.125 blade chord sized elements in this region. The entire computational domain is comprised of approximately 170 million elements for side-by-side cases, with 50 million in each rotating volume, and 70 million in the surrounding nonrotating volume. In previously published grid refinement studies, these rotor mesh parameters have been found to provide spatial convergence to within 1.2% integrated thrust and 1.6% integrated torque (Refs. [3, 4]). The mesh parameters are also consistent with those used in Ref. [1] which were found to be spatially converged. The blade mesh parameters are also similar to other unstructured rotorcraft simulations such as Refs. 2, 48, and 51.

A delayed detached eddy simulation (DDES) is used with the Spalart–Allmarus turbulence model on-body for all simulations. Each case is initially run using time steps corresponding to 10° of rotation for at least 40 revolutions in order to reduce the computational cost of rotor wake –development. These initial 10° time steps are possible without numerical divergence due to the stability afforded by the streamline upwind Petrov–Galerkin stabilized finite element method and generalized α implicit time integration method. The latter method was designed to suppress high-ins frequency disturbances and allow solution stability with Courant–Friedrichs–Lewy number greater than 1 (Refs. [25, 52]). Following the revolutions simulated with 10° time steps, an additional five revolutions (at minimum) are performed with time steps corresponding to 1° with sufficient subiterations to reduced residuals by two orders of magnitude. Based on results presented in the Appendix, time steps corresponding to 1° of rotor rotation are deemed sufficient, with integrated thrust and torque differing by less than 1% to a solution computed with 0.5° time steps. When extracting steady integrated loads, the average rotor forces and moments over the final three revolutions are considered. However, for some cases, additional revolutions must be simulated in order to more fully observe low-frequency load fluctuations. If the single revolution running averaged thrust for either rotor is found to change by more than 1% over three revolutions, additional revolutions are simulated. For sectional thrust coefficient disk plots, loads are also phase-averaged between the three rotor blades. All runs are performed on eight

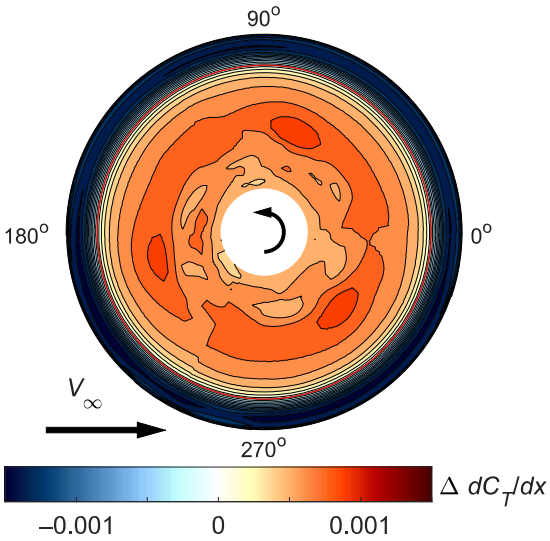

Fig. 5. Sectional thrust coefficient difference between a single IGE rotor at H/D = 0.5 and an OGE rotor (IGE minus OGE).

24-core AMD Epyc 7451 processors, part of the Center for Computational Innovations at Rensselaer Polytechnic Institute.

Results

Isolated rotors in ground effect

As a point of reference for side-by-side rotor performance IGE, a single hovering rotor IGE at H/D = 0.5 is first simulated, and its performance is compared to a rotor hovering OGE. Figure 5 shows the difference in sectional thrust coefficient between the two cases (IGE minus OGE). Here, red represents an increase in thrust compared to OGE, and blue represents a thrust deficit compared to OGE. Thrust increment is observed on the interior of the disk (from the root to 0.85R), whereas thrust deficit is observed near the tips. Overall, integrated rotor thrust IGE at H/D = 0.5 is 6.4% greater than OGE (684.3 N IGE vs. 643.4 N OGE), making the IGE/OGE thrust ratio $T_{\text{IGE}}/T_{\text{OGE}} = 1.064$. This ratio is similar to that predicted by Cheeseman and Bennett ($T_{\text{IGE}}/T_{\text{OGE}} = 1.067$) (Ref. [53]). The integrated rotor torque produced IGE at H/D = 0.5 is found to be within 1.2% of that produced OGE (61.3 Nm IGE vs. 60.6 Nm OGE).

The presence of a ground plane influences rotor performance by changing the wake aerodynamics. Figure 6 shows a slice through the hub colored by vertical velocity for OGE and IGE (H/D = 0.5) cases with velocity direction vectors. For the OGE case, the dark blue wake freely convects downwards. When the ground plane is introduced, however, the wake impinges on the ground plane. The wake's tip vortices impact the ground and spread outward radially. Inside the wake, flow is constrained by both the ground plane and the outboard wake. With nowhere to go, the inboard section of the flow fountains upwards around the hub region. Fountaining around the hub region and through the central region of the rotor disk has been reported on other rotors IGE and is attributed to root vortices converging to the center of rotation and traveling vertically upwards (Refs. [9, 54]). Within the fountaining region, strong turbulence is observed with many vortical structures mixing and interacting. The stochastic nature of this fountaining flow leads to the IGE rotor's azimuthal thrust variations in Fig. 5.

The relationship between wake structure and thrust production can be seen by looking at vertical velocity over the rotor disk. Figure 7 shows

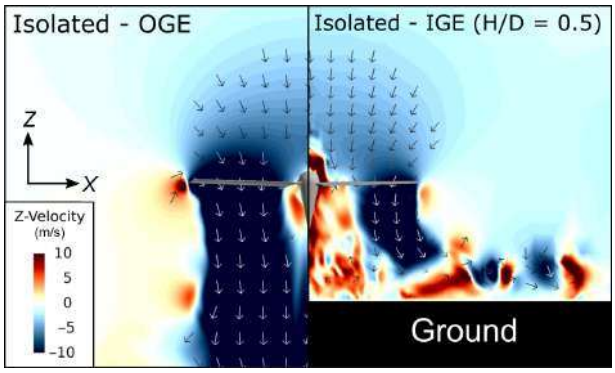

Fig. 6. Slice colored by vertical velocity for OGE and IGE (H/D = 0.5) rotors.

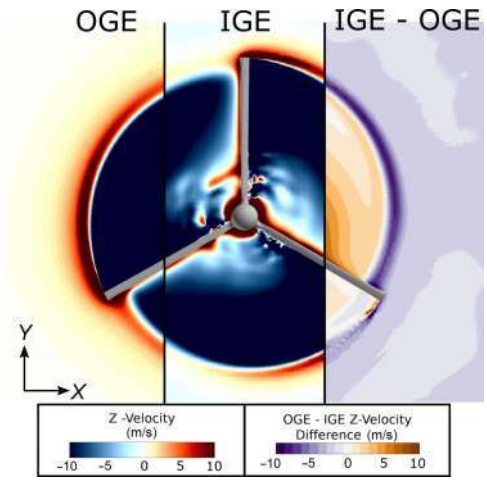

Fig. 7. Vertical velocity through OGE and IGE (H/D = 0.5) rotor disks, as well as vertical velocity difference (IGE minus OGE) at the rotor plane.

vertical velocity at the rotor plane for OGE and IGE (H/D = 0.5) rotors. The vertical velocity difference between the cases (IGE minus OGE) is also shown. On the inboard sections of the blade, a positive difference in velocity is observed (orange portion of the rightmost slice in Fig. 7). With the two left vertical velocity plots showing downward velocity (blue) in this region, this indicates a reduction in downwash induced by the IGE rotor (compared to the OGE rotor). Fountaining on the inboard regions of the rotor induces relative upwash on the inboard blade sections. Upwash on inboard blade sections leads to an increase in the angle of attack and the relative increase in thrust observed in Fig. 5. The IGE rotor shows a thrust deficit over the tip region (see the dark blue peripheral ring at radial stations outboard of 85% in Fig. 5). This is a result of higher downwash at the blade tips (see the dark purple region on the right slice of Fig. 7) and can be attributed to the recirculating flow IGE.

An isolated (single) rotor IGE at H/D = 1 is also simulated. Figure 8 shows a slice through the hub colored by vertical velocity for IGE (H/D = 1) and IGE (H/D = 0.5) cases. Like with the rotor at H/D = 0.5, the wake generated by a rotor IGE at H/D = 1 convects downwards until it hits the ground plane and proceeds to spread radially. Flow on the inboard portion of the wake is still constrained from exiting the system by the outboard wake section, leading to strong turbulence, but is too far below the rotor to fountain through the disk plane.

Without the flow fountaining through the central region of the rotor disk, the thrust distribution of the rotor at H/D = 1 is different than that

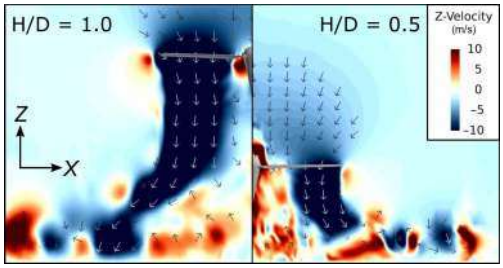

Fig. 8. Slice cutting through the hub of H/D = 1 IGE and H/D = 0.5 IGE rotor hubs colored by vertical velocity.

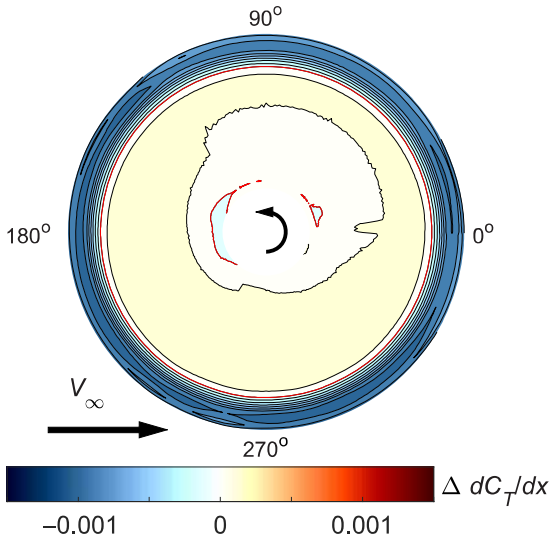

Fig. 9. Sectional thrust coefficient difference between a single rotor IGE rotor at H/D = 1, and an OGE rotor (IGE minus OGE).

at H/D = 0.5. Figure 9 shows the sectional thrust coefficient difference between a rotor IGE (H/D = 1) and a rotor OGE (IGE minus OGE). Without fountaining reaching the disk plane, the IGE rotor at H/D = 1 does not show the significant thrust increment on the inboard sections that were observed for the H/D = 0.5 case in Fig. 5). Like the isolated IGE rotor at H/D = 0.5, moderate thrust deficit is observed near the blade tips due to recirculating flow, but this too is weaker than the H/D = 0.5 case in Fig. 5 (same color scale used on Figs. 5 and 9). Overall, including the teardrop hub forces, a 0.5% increase in thrust is observed for the H/D = 1 rotor compared to OGE (646.7 N IGE vs. 643.4 N OGE). Similarly, torque remains within 1.0% of the OGE rotor (61.3 Nm IGE vs. 60.6 Nm OGE).

Side by side H/D = 0.5

Simulation of side-by-side rotors at H/D = 0.5 and 3.0R hub–hub separation is presented next. Figure 10 shows a direct volume rendering of vorticity magnitude for side-by-side rotors at 3R separation. Portions of the flow field with greater vorticity magnitude are rendered with greater opacity. Tip paths for each rotor are annotated as red rings. A red grid is also plotted parallel to the $\psi = 90°$–$270°$ line between the rotors which extends from the ground plane to 1R above the rotor plane. From $\psi = 270°$ to 90° (through 0° in the direction of rotation), the right rotor wake has a similar structure to that of a single rotor. Tip vortices convect down and impact the ground, then move radially away from the rotor. On the side of the disk facing the other rotor, however, the flow

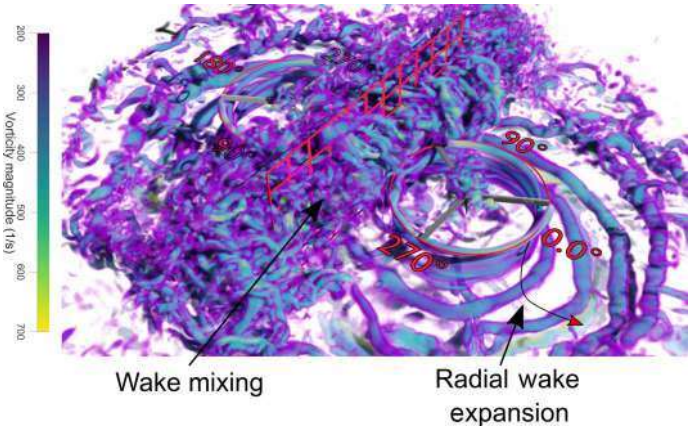

Fig. 10. Direct volume rendering of H/D = 0.5, 3.0R separation side-by-side rotors with opacity and color dictated by vorticity magnitude.

from the two rotors collides and the flow is constrained from moving radially. Where the wakes collide, mixing produces a wall of strong turbulence between the rotors, in the interrotor region. This wall extends upwards and outwards (laterally) and intersects the tip-path-plane of the rotors (covering both the red tip-path-plane rings and the middle red grid). Similar effects have been observed on tilt-rotors in hover, where spanwise flow over the wing has been shown to fountain over the centerline of the vehicle and fluctuate left and right over many revolutions. Reingestion of the fountained flow has been reported to reduce rotor performance near the tips and induce impulsive loading (Refs. [30–33]). In this case, however, the extents of the ground plane are not limited to the chordwise extents of a wing, and so the region of fountaining flow extends farther outward laterally than that observed on tiltrotor wings.

Figure 11 shows the difference in sectional thrust coefficient between the two IGE rotors and an OGE single rotor (IGE minus OGE), phase averaged over three revolutions. Thrust increment inboard and thrust deficit outboard are observed like with the single rotor IGE case. However, with the presence of two rotors, larger thrust losses are observed at the tips when the blades pass between the rotors (compare the region around $\psi = 180°$ on the right rotor in Fig. 11 to the region around $\psi = 0°$). On the right rotor at $\psi = 180°$, dC_T/dx is 0.0038 less than an isolated OGE rotor, whereas at $\psi = 0$, dC_T/dx is only 0.0014 less. Similar interrotor thrust deficits have been reported on nearby rotors OGE, but these effects have been shown to be small, reducing integrated thrust by less than 2% (Refs. [7, 55]). Interrotor thrust losses are greater IGE, with dC_T/dx between the rotors reducing by up to 39.9% (compared to if the rotor was operating in isolation). The losses are also dissimilar in distribution between the rotors and change from revolution to revolution due to the highly chaotic vortical flow in the interrotor region.

The unsteady thrust produced by side-by-side rotors IGE suggests interactional aerodynamics between the rotors. Figure 12 shows a slice cutting through both rotor hubs colored by vorticity in the $+Y$ direction (into the page). Velocity direction vectors are also shown. On the outsides of the system, tip vortices are observed to move downwards, then outward radially upon impacting the ground (similar to a single rotor IGE). Between the rotors, however, substantial wake mixing is observed. The wakes of each rotor collide in the middle to produce a highly turbulent vortical flow with substantial mixing. As each blade passes through the interrotor region, it intersects with the vortical flow between the rotors. Tip vortices generated between the rotors are pulled into the mixing region, adding vorticity to the flow and perpetuating the turbulent nature of the region. When simulated with a finer interrotor grid, similar features are still observed, as discussed in more detail in the Appendix. In both

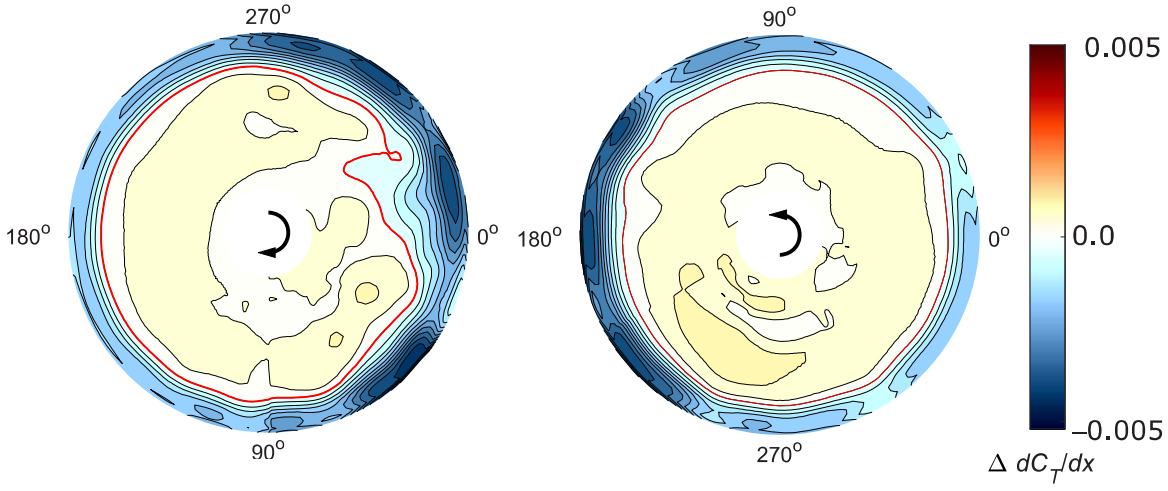

Fig. 11. Three revolution average sectional thrust coefficient difference between side-by-side H/D = 0.5 rotors with 3.0*R* spacing and a single rotor OGE rotor (IGE minus OGE).

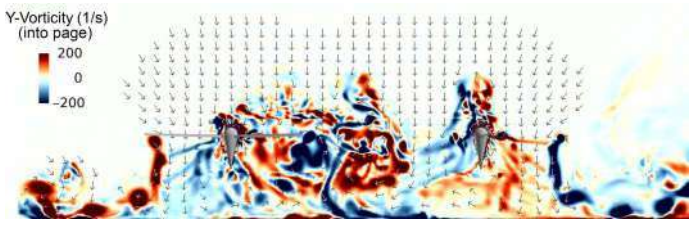

Fig. 12. Slice cutting through side-by-side H/D = 0.5 3.0*R* separation IGE rotor hubs colored by Y-vorticity.

cases, turbulent mixing flow fountains above the rotors and intersects with the disk planes. As the blades pass through the turbulent mixing, impulsive loading is induced.

Figure 13 shows the thrust history for each side-by-side rotor at H/D = 0.5 and 3.0*R* separation normalized by isolated OGE rotor thrust. Running average thrust over one revolution is also presented for each rotor as well as average thrust between the two rotors. Substantial unsteady loading is observed for both rotors as blades pass through the center mixing region, with peak-to-peak fluctuations in excess of 10% of the steady thrust. Average thrust over one revolution is not steady, with the left rotor average thrust changing by greater than 5% over the revolutions plotted (and the right rotor changing by 3%). The relative mean thrust between rotors changes as well, with the left rotor producing more thrust at certain revolutions, and the right rotor producing more at others (depending on the predominant position of the unsteady vortical flow in the interrotor region). Average thrust of both rotors is relatively stable, only changing by approximately 2% over these seven revolutions. Overall, the thrust increment gained inboard is canceled by thrust deficits incurred between the rotors. Averaging over three revolutions (and averaging between both left and right rotors), the side-by-side rotors at H/D = 0.5 with 3.0*R* spacing produce comparable thrust (642.0 N) to a single rotor OGE (643.4 N). The torque produced by each side-by-side rotor IGE is also found to be similar to that produced by an OGE rotor, with the average integrated torque between both left and right rotors lying within 0.3% of that produced OGE (60.8 Nm IGE vs. 60.6 Nm OGE).

Changes in mean thrust from revolution to revolution are caused by pockets of strong vorticity moving within the mixing region at a rate slower than 1/rev. Figure 14 shows a slice cutting through both rotor hubs colored by vorticity magnitude with velocity streamlines. The top

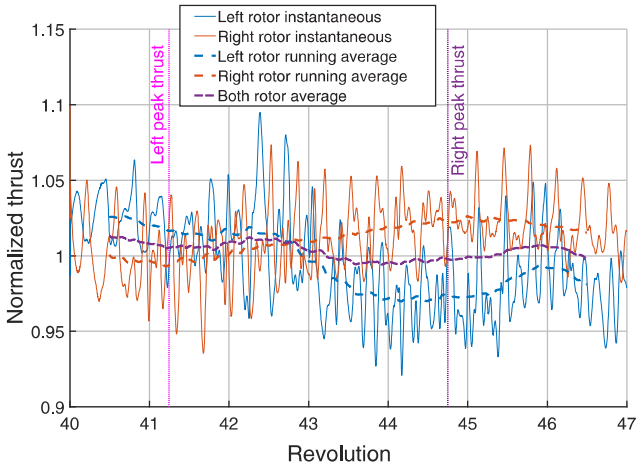

Fig. 13. Thrust history of each side-by-side rotor at H/D = 0.5 and 3.0*R* hub–hub separation, including instantaneous, single rotor rev-averaged thrust and both rotor rev-averaged thrust normalized by isolated OGE rotor thrust.

half corresponds to a time in the simulation when the left rotor produces more thrust (magenta line in Fig. 13), and the bottom corresponds to when the right rotor produces more thrust (purple line in Fig. 13). When the left rotor is producing greater thrust, vortical mixing between the rotors has fountained up and over the right rotor and the left rotor avoids the strongest turbulence. In contrast, when the right rotor is producing greater thrust, a majority of the vorticity is above the left rotor where it has a stronger detrimental influence on the left rotor's performance.

The harmonic content of the blade loading depends on the relative position of the vortical mixing between the rotors. For example, between revolutions 45 and 46 in Fig. 13 when the right rotor is producing more thrust, most of the turbulent mixing is away from the right rotor (bottom of Fig. 14), and a predominantly 3/rev signal is observed. During the same time period however (between revolutions 45 and 46), the left rotor is subject to the mixing flow and produces higher frequency thrust fluctuations (Fig. 13). In general, when the vortical mixing is closer to a given rotor, it has a wider range of azimuths over which its blades will encounter turbulence and produces higher frequency unsteady loads.

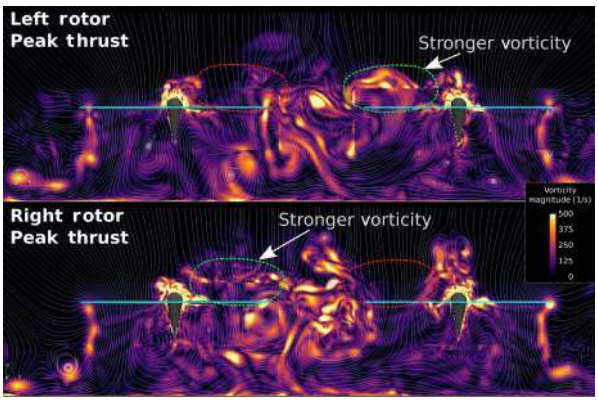

Fig. 14. Slice cutting through side-by-side H/D = 0.5 3.0*R* separation IGE rotor hubs colored by vorticity magnitude at two different time steps with white velocity streamlines. Discontinuities at the sliding mesh interface are due to grid misalignment in the visualization file. When probed directly from the solution, no flow discontinuity is observed.

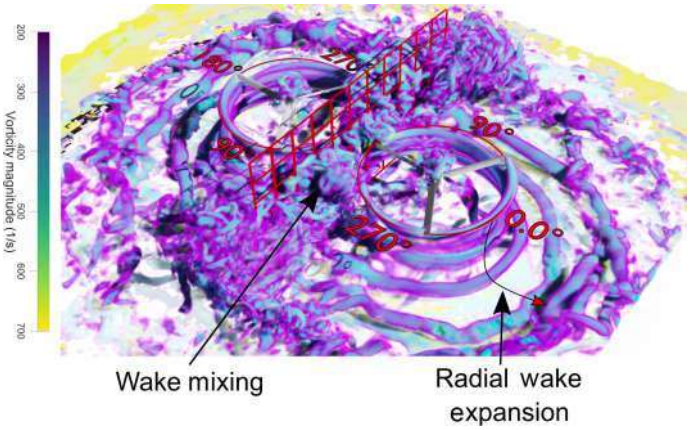

Fig. 15. Direct volume rendering of side-by-side rotors at H/D = 0.5 and 2.5*R* separation with opacity and color dictated by vorticity magnitude.

This characteristic is discussed further in the Appendix, where thrust signals are decomposed into the frequency spectrum. Beyond changes in dominant frequency, the variability of unsteady loading is notable as well with peak-to-peak changes in instantaneous thrust varying from 6% up to 11%.

Another side-by-side rotor system at H/D = 0.5 is also simulated with 2.5*R* rotor–rotor spacing. Figure 15 shows direct volume rendering of vorticity magnitude for side-by-side rotors with closer 2.5*R* spacing. Tip paths for each rotor are displayed as red rings. A red grid is also plotted parallel to the $\psi = 90°$–$270°$ line between the rotors. Just as when the rotors had 3.0*R* hub–hub separation, the wake of the right rotor from $\psi = 270°$ to $90°$ behaves much the same way as the isolated H/D = 0.5 wake. However, between the rotors, wake mixing for the 2.5*R* separation case is weaker than with 3.0*R* separation and occupies a lesser portion of the domain. Whereas mixing for the 3.0*R* separation case in Fig. 10 reaches above the top of the grid (1.0*R* above the rotor plane), the mixing with 2.5*R* separation only reaches one square above the disk plane (1/3*R* above). Strong vorticity also covers less of the tip path plane, indicating blades will encounter strong vorticity over a smaller range of azimuths.

Figure 16 shows the difference in sectional thrust coefficient between two H/D = 0.5 IGE rotors with 2.5*R* hub–hub separation and an OGE single rotor (IGE minus OGE), averaged over three revolutions. Like the other H/D = 0.5 case shown in Fig. 11, thrust increment is observed inboard. Thrust deficit is observed near the tips and is significantly stronger between the rotors. Again, strong turbulence in the mixing region between rotors leads to thrust losses when blades pass through.

Figure 17 shows a slice colored by vorticity magnitude cutting through both side-by-side rotor hubs at H/D = 0.5 with 2.5*R* hub–hub separation. The tip paths of both rotors are annotated in cyan. The mixing between the rotors for this does not intersect with the rotors as significantly as observed in Fig. 14. The turbulence remains relatively stationary from revolution to revolution in the interrotor region and does not fountain over the disk plane as in Fig. 14. Whereas the 3.0*R* separation case saw strong vorticity magnitude fountaining onto inboard portions of the disks, only the blade tips encounter the turbulent mixing region at 2.5*R* separation. Additionally, with blade tips only separated by 0.5*R*, the turbulent mixing does not have room to move side-to-side closer to one rotor over the other.

With a majority of the thrust deficit on only one side of the disk (as seen in Fig. 16), periodic loading is induced. Figure 18 shows the thrust history for each side-by-side rotor at H/D = 0.5 and 2.5*R*

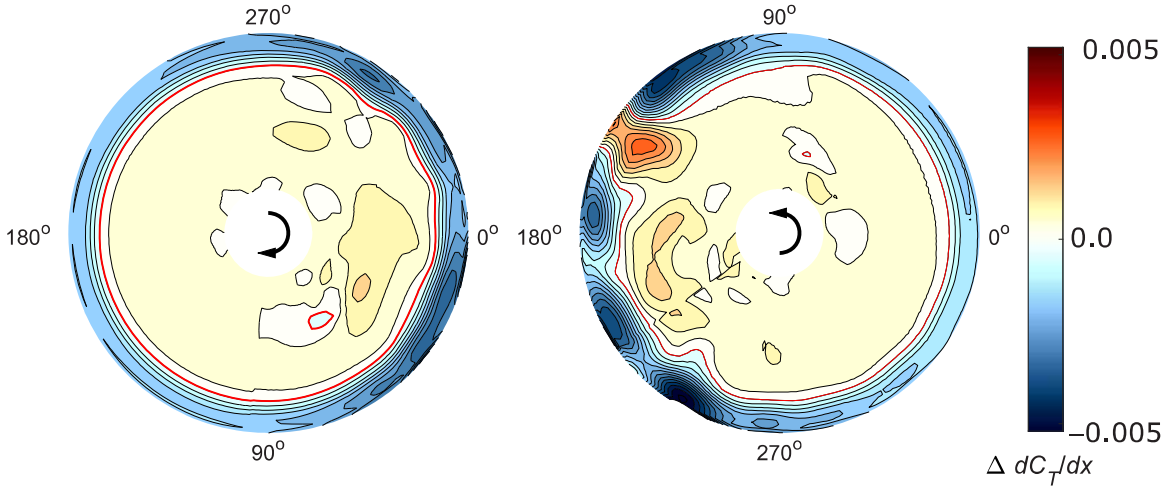

Fig. 16. Three revolution average sectional thrust coefficient difference between side-by-side H/D = 0.5 rotors with 2.5*R* spacing and a single OGE rotor.

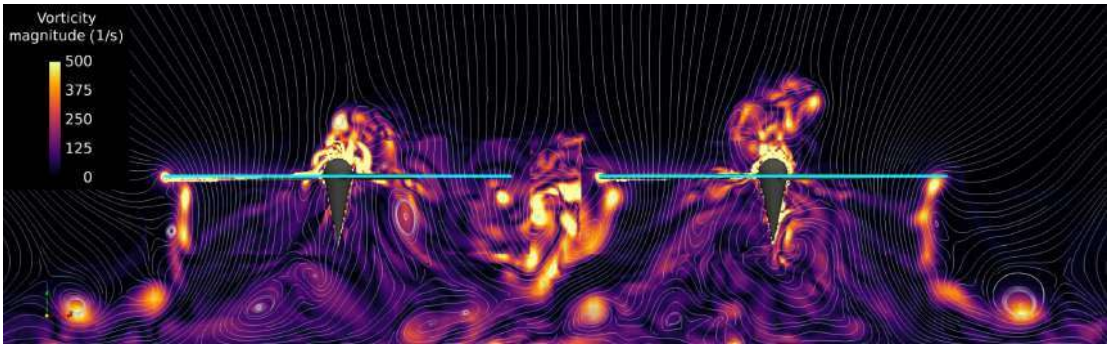

Fig. 17. Slice cutting through side-by-side H/D = 0.5 2.5*R* separation IGE rotor hubs colored by vorticity magnitude. Discontinuities at the sliding mesh interface are due to grid misalignment in the visualization file. When probed directly from the solution, no flow discontinuity is observed.

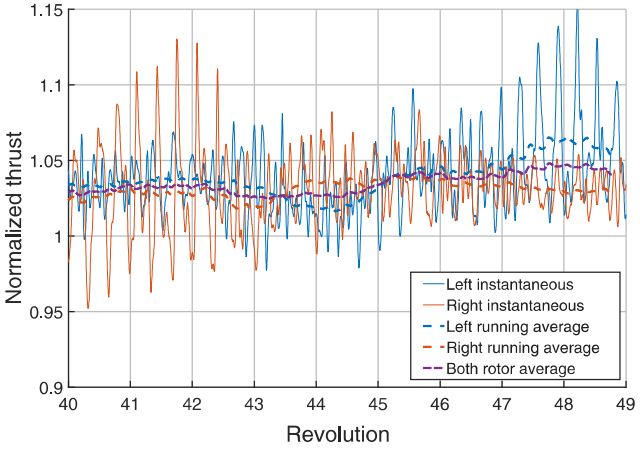

Fig. 18. Thrust history of each side-by-side rotor at H/D = 0.5 and 2.5*R* hub–hub separation, including instantaneous, single rotor rev-averaged thrust, and both rotor rev-averaged thrust normalized by isolated OGE thrust.

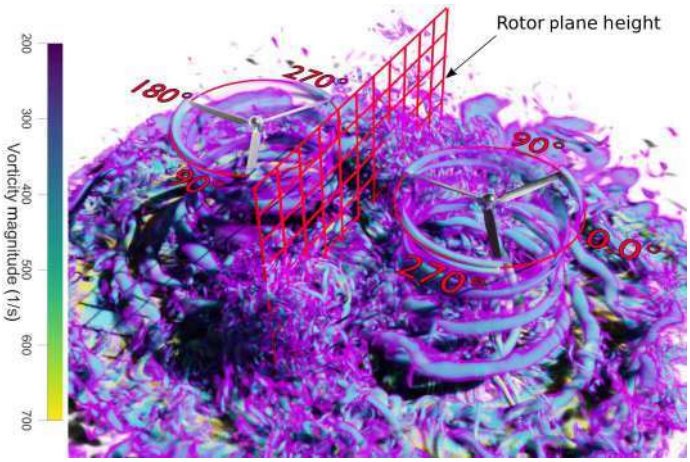

Fig. 19. Direct volume rendering of H/D = 1, 3.0*R* separation side-by-side rotors with opacity and color dictated by vorticity magnitude.

separation normalized by isolated OGE rotor thrust. Single rotor running rev-averaged thrust over time as well as both rotor running rev-averaged thrust is also plotted. Unsteady loading for these rotors is substantial, with instantaneous thrust oscillating peak-to-peak up to 16% from the running average. Three per-rev loading due to blade passage through a nonuniform flow field (mainly between the rotors) is clearly observed. Unsteady loading at 3/rev is slightly stronger at 2.5*R* separation than 3.0*R* separation as seen in by comparing Figs. 13–18. This could be attributed to blade tips at 2.5*R* encountering a concentrated mixing region, whereas the blade tips and inboard regions at 3.0*R* separation encounter more dispersed vortical mixing.

Average thrust for the 2.5*R* separation rotors is not steady from revolution to revolution either. Single revolution average thrust for the left rotor changes by almost 5% over the period simulated and the right rotor by 2%. Due to the stochastic nature of the flow, it is expected that if additional revolutions were simulated, the average thrust fluctuations would be similar for both the left and right rotors. The average thrust difference between rotors is less than that observed when separation was 3.0*R*. With less substantial thrust losses between the rotors, thrust increment inboard leads to a net thrust improvement compared to OGE. Averaging over three revolutions (and averaging between both left and right rotors), the side-by-side rotors at H/D = 0.5 with 2.5*R* spacing produce 4.3% more thrust than a single rotor OGE (670.8 N IGE vs. 643.4 N OGE), but 2.4% less thrust than an isolated rotor at H/D = 0.5 (670.8 N side-by-side vs. 687.5 N isolated).

Side by side H/D = 1

Side-by-side rotors are also simulated higher from the ground, at H/D = 1. Figure 19 shows direct volume rendering of vorticity magnitude for side-by-side rotors at H/D = 1 and 3.0*R* hub–hub separation. The red grid between the rotors extends 1*R* above the rotor plane and to the ground (2*R*) below. From $\psi = 270^\circ$ to 90° (through 0°), the right rotor wake convects downwards until it impacts the ground and spreads radially. Between the rotors, the wake still convects downwards until it reaches close to the ground. Instead of moving radially along the ground, however, the wake of each rotor impinges on the other and mixes near the ground plane. The wake mixing remains primarily within one rotor radii of the ground plane and does not reach the rotor plane.

Figure 20 plots sectional thrust coefficient difference between an isolated OGE rotor and side-by-side rotors at H/D = 1 and 3.0*R* separation. Relative to the rotors at H/D = 0.5, there is minimal thrust difference inboard as the rotors are too high off the ground to encounter significant fountaining over the inboard sections. Like with the isolated IGE rotor at H/D = 1, thrust deficit is observed near the blade tips but it is much weaker than the H/D = 0.5 case. The thrust deficit is again highest between the rotors. Some modest asymmetry in thrust distribution is observed between the rotors, with the left rotor distribution

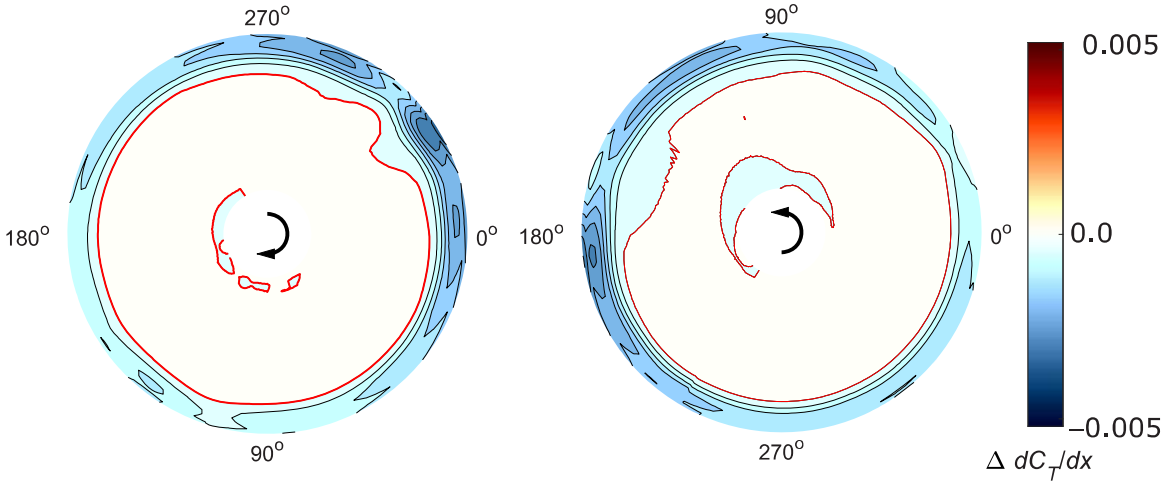

Fig. 20. Three revolution average sectional thrust coefficient difference between side-by-side H/D = 1 rotors with 3.0*R* spacing and a single OGE rotor (IGE minus OGE).

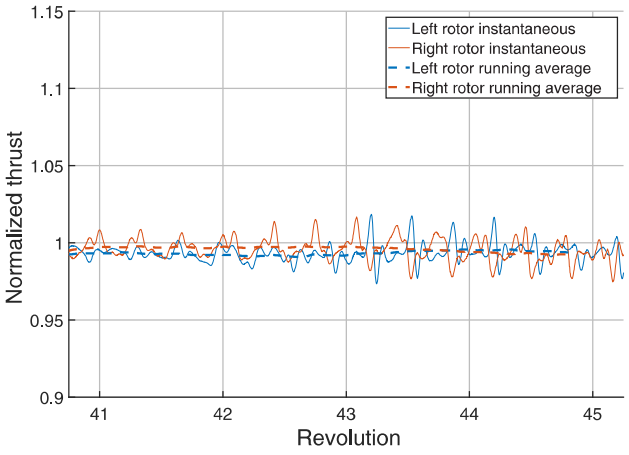

Fig. 21. Thrust history of each side-by-side rotor at H/D = 1 and 3.0*R* hub–hub separation, including instantaneous, single rotor rev-averaged thrust, and both rotor rev-averaged thrust normalized by isolated OGE thrust.

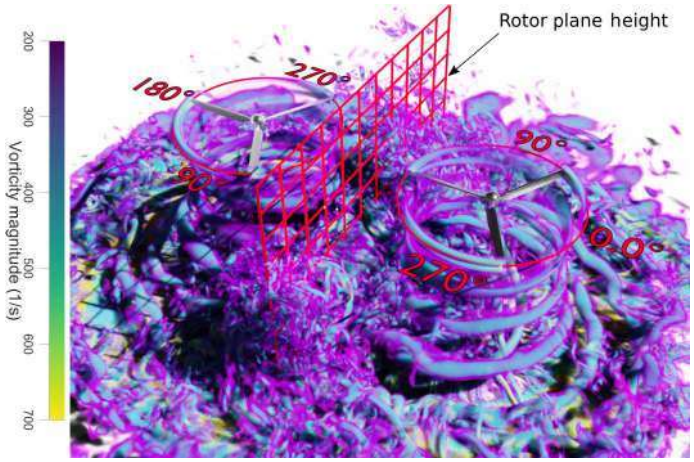

Fig. 22. Direct volume rendering of H/D = 1, 2.5*R* separation side-by-side rotors with opacity and color dictated by vorticity magnitude.

in Fig. 20 not being equal to a mirror image of the right rotor distribution. This can be attributed to the relatively weak (but nonzero) influence of the turbulent mixing between the rotors. The presence of 3/rev loading (to be discussed with Fig. 21) also indicates that blades at H/D = 1 encounter some nonuniform flow attributed to turbulence between rotors (albeit to a lesser extent than that seen when rotors are positioned at H/D = 0.5). The stochastic nature of the turbulence between the rotors can be expected to introduce the asymmetries in the thrust distribution present in Fig. 21.

While some small thrust asymmetries are observed for side-by-side rotors at H/D = 1, they produce lesser unsteady loading than at H/D = 0.5. Figure 21 plots the thrust history of each side-by-side rotor at H/D = 1 with 3.0*R* hub–hub separation normalized by isolated OGE thrust. Running average thrust over one revolution is also plotted for each rotor. Peak-to-peak loading up to 4% mean thrust is observed, significantly less than at H/D = 0.5. Reduced unsteady loading is attributed to the turbulent mixing region between the rotors staying below the rotor plane. However, the 4% peak–peak loading that is present is not observed on the isolated rotor at H/D = 1, suggesting some turbulent mixing still induces unsteady loading. Mean thrust for rotors at H/D = 1 is relatively constant and does not vary from revolution to revolution like rotors at H/D = 0.5. Including the teardrop hubs, mean thrust for these rotors is consistently within 0.6% of an isolated OGE rotor (639.7 N IGE vs. 643.4 N OGE).

Side-by-side rotors at H/D = 1 with 2.5*R* hub–hub separation are also simulated. Figure 22 shows direct volume rendering of vorticity magnitude for side-by-side rotors at H/D = 1 and 2.5*R* hub–hub separation. Like the other IGE rotors, the wake from $\psi = 270°$ to 90° through 0° convects radially after impacting the ground. Between the rotors, the wakes collide approximately 1*R* above the ground. With less space between the rotors for mixing to develop, the turbulent region does not extend as high as that observed at H/D = 1 and 3*R* separation.

Thrust losses and oscillatory loads for side-by-side rotors at H/D = 1 and 2.5*R* hub–hub separation are similar in distribution and magnitude to those observed at 3.0*R* hub–hub separation (Figs. 23, 24). No thrust increment is observed inboard, and a lower thrust deficit is seen between the rotors than the H/D = 0.5 case. Thrust distribution asymmetries like those observed in Fig. 20 are also observed due to the modest influence of turbulent mixing between the rotors. This is corroborated by the presence of lower magnitude 3/rev loading in Fig. 24 that is not present on the

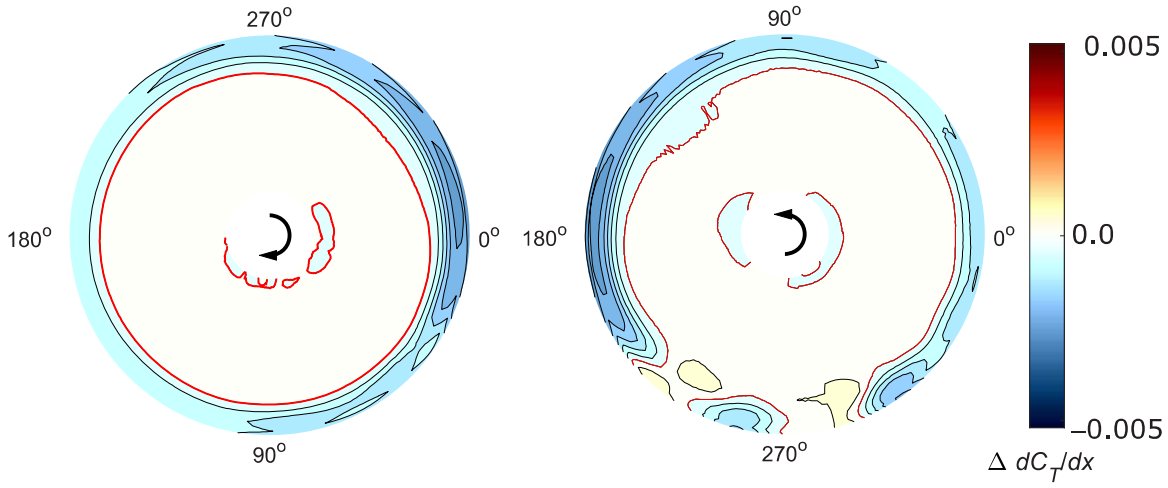

Fig. 23. Three revolution average sectional thrust coefficient difference between side-by-side H/D = 1 rotors with 2.5*R* spacing and a single OGE rotor (IGE minus OGE).

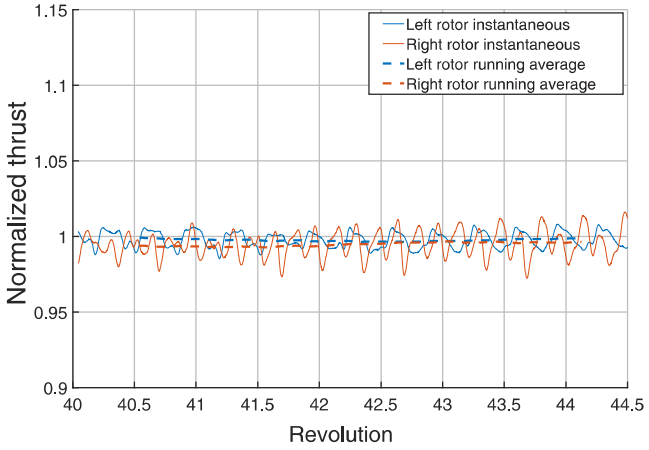

Fig. 24. Thrust history of each side-by-side rotor at H/D = 1 and 2.5*R* hub–hub separation, including instantaneous, single rotor rev-averaged thrust, and both rotor rev-averaged thrust normalized by isolated OGE thrust.

isolated rotor at H/D = 1. Unsteady loading has peak-to-peak values up to 4% of mean thrust. Mean thrust does not show much variation and is within 0.3% of an isolated OGE rotor (641.3 N IGE vs. 643.4 N OGE), and 0.8% less than an isolated H/D = 1.0 rotor (641.3 N side-by-side vs. 646.7 N isolated). Mean thrust for each rotor is relatively steady with time.

Integrated load comparison

Interactional aerodynamics has been seen to influence the thrust performance of side-by-side rotors IGE. Table 2 compares time-averaged integrated thrust for all six IGE cases discussed. Thrust values are presented relative to the thrust generated by an isolated OGE rotor. An isolated rotor at H/D = 0.5 provides the greatest thrust increase, producing 6.5% more thrust than if OGE. If positioned higher at H/D = 1.0, the effect of the ground on rotor-induced velocity lessens and decreased fountaining passes through inboard disk regions, leading to reduced thrust increment. Despite receiving thrust increment inboard, side-by-side rotors at H/D = 0.5 with 3.0*R* hub–hub spacing produce less thrust than

Table 2. Relative thrust difference between six IGE rotor cases and an isolated OGE rotor (IGE minus OGE)

Isolated 1.0 H/D	0.5%
Isolated 0.5 H/D	6.4%
Side-by-side 0.5 H/D 3.0*R*	−0.2%
Side-by-side 0.5 H/D 2.5*R*	4.3%
Side-by-side 1.0 H/D 3.0*R*	−1.5%
Side-by-side 1.0 H/D 2.5*R*	−0.3%

an isolated OGE rotor. Thrust deficits in the region of the blade tips, especially in the region between the rotors where there is turbulent mixing, negate any inboard thrust increment, leading to a net loss in thrust. Less outboard thrust deficit is observed between side-by-side rotors IGE at H/D = 0.5 and relatively smaller 2.5*R* hub–hub spacing, leading to some net increment in steady integrated thrust. Overall, these rotors produce 4.5% more thrust than an isolated OGE rotor; however, the increase is less than that observed for an isolated rotor at the same height above the ground due to the blades still encountering turbulent mixing between the rotors. Side-by-side rotors at H/D = 1 do not see any lift increment from fountaining through the hub region and show a small thrust deficit (of up to 0.6%) due to lift loss between the rotors.

Substantial unsteady loading has also been shown for side-by-side rotors IGE. Table 3 compares the amplitude of impulsive loading for each IGE case by presenting the maximum peak-to-peak change in rotor thrust, normalized by mean steady thrust. Isolated rotors, both at H/D = 0.5 and H/D = 1.0, produce relatively steady thrust, whereas side-by-side rotors generally produce substantial unsteady loading. Peak-to-peak thrust oscillations are observed to be strongest at H/D = 0.5 (15.5%) when the rotors operate close to the ground and intersect with a concentrated turbulent mixing region. Overall, the amplitude of unsteady loading for side-by-side rotors at H/D = 0.5 is on the order of four times that produced at H/D = 1.0. (4.1%, 3.5%)

The relationship that hub–hub spacing has with maximum peak-to-peak loading depends on the height above the ground. At H/D = 0.5, the maximum peak-to-peak loading for rotors operating closer together at 2.5*R* hub–hub separation is almost 5% greater than when rotors have 3.0*R* separation. At H/D = 1.0, however, the rotors do not directly interact with the turbulent mixing region and the influence of hub–hub separation is less pronounced. Rotors at 3.0*R* hub–hub separation at H/D = 1.0 produce very slightly stronger maximum peak-to-peak loads

Table 3. Peak-to-peak impulsive loading for rotors IGE normalized by mean steady thrust

Isolated 0.5 H/D	1.3%
Isolated 1.0 H/D	0.7%
Side-by-side 0.5 H/D 3.0*R*	10.8%
Side-by-side 0.5 H/D 2.5*R*	15.5%
Side-by-side 1.0 H/D 3.0*R*	4.1%
Side-by-side 1.0 H/D 2.5*R*	3.5%

than 2.5*R* separation. In general, peak-to-peak loading tends to trend with the strength of the turbulent mixing region that intersects with the rotor disk.

Outwash Comparison

When the wake of an isolated rotor IGE impacts the ground, it is able to freely convect radially away from the rotor. As the wake skirts along the ground, it induces a net radial velocity. This can be seen for isolated rotors at H/D = 0.5 and H/D = 1 in Fig. 25. This figure plots an unwrapped cylinder extending from the ground plane to a height of 1.25D (2.5*R*) around an isolated rotor or the right rotor of the two rotor systems considered in this study. The colors indicate the magnitude of the instantaneous radial velocity. The cylinder radius extends 1.25*R* for the isolated rotors and to the middle (symmetry plane) of the side-by-side rotors. Thus, the cylinder radius is 1.25*R* or 1.5*R* depending on whether the hub-to-hub separation is 2.5*R* or 3*R* respectively, for the two rotor cases. The cylinder (diagrammed in the bottom-left) is unwrapped to form a 2D plane. A magenta line is plotted along the projection of the tip path plane. For the isolated rotors, a skirt of radial velocity exceeding 20 m/s is observed within 0.25D of the ground.

When a second, nearby rotor is introduced (in the side-by-side configuration), the wakes of each rotor interfere with each other. Outside the rotors ($\psi = 270°$–$360°$ and $0°$–$90°$), the same radial velocity is seen as with the isolated rotors. Between the rotors, however, wake mixing leads to radial velocity being bidirectional (into or out of the cylinder). The mixing regions for 3.0*R* separation cases tend to occupy a larger range of azimuths than 2.5*R* separation cases. Rotors at H/D = 1 operate primarily above the mixing region.

Figure 26 shows the same unwrapped cylinders as Fig. 25 but colored by vertical velocity. The downwards vertical velocity observed for the isolated cases near the ground is the result of a tip vortex outside the cylinder locally inducing downwash at the radial location and time instant plotted. For side-by-side rotor cases, only moderate vertical velocity is induced away from the other rotor ($\psi = 270°$–$360°$ and $0°$–$90°$). In the mixing region between the rotors ($\psi = 90°$–$180°$–$270°$), predominantly upwash is induced as the rotor wakes collide and fountain. For side-by-side rotors at H/D = 0.5, this upwash extends above the rotor disk planes (annotated in magenta), but for rotors at H/D = 1 it remains below the rotor plane height.

In the interrotor region, while the colliding wakes result in part of the flow moving upward (vertical fountain), a substantial part of the flow leaves that region laterally (sideways, in the $\pm Y$ direction). Figure 27 shows slices positioned equally between side-by-side rotors colored by Y-velocity. Blue indicates velocity moving towards the right rotor's $\psi = 270°$ direction and red towards the right rotor's $\psi = 90°$ direction. For all side-by-side cases, the flow between the rotors cannot move radially as when they were in isolation and instead must move upward and laterally to escape the system. Lateral outwash for all cases is as strong (exceeding 20 m/s) as the radial outwash for the isolated rotors and extends higher vertically above the ground plane. While the skirt of radial velocity for an isolated rotor only extends 0.25D above the ground, lateral flow for the side-by-side rotors in Fig. 27 is observed to propagate up to 1D above the ground plane.

Conclusions

This study investigates the interactional aerodynamics of side-by-side rotors IGE. The computational fluid dynamics code AcuSolve®, with DDES, was used to simulate the aerodynamics of the system. The sliding mesh method was used to simulate blade motion by interfacing two rotating volumes (one for each rotor) within a nonrotating volume. Every simulation was performed with 5.5 ft diameter, three-bladed rotors with uniform planform and linearly twisted blades spinning at 1600 RPM, corresponding to a 5-lb/ft^2 target disk loading OGE. In all, seven cases were simulated: isolated OGE, isolated IGE at H/D = 0.5 and H/D = 1, side-by-side rotors at H/D = 0.5 with 3.0*R* and 2.5*R* hub–hub separation, and side-by-side rotors at H/D = 1 with 3.0*R* and 2.5*R* separation. The performance of isolated and side-by-side rotors IGE was compared to the performance of an isolated OGE rotor. Through these simulations, the following observations were made.

1) Between side-by-side rotors IGE, the wakes of each rotor collide, inducing turbulent mixing that can fountain up, through, and over the rotor disk plane.

2) For the side-by-side rotors, thrust penalties are observed over the outboard sections of the blades particularly as they pass through the interrotor region. For IGE rotors at 3.0*R* hub–hub separation, thrust production is similar to OGE operation with interrotor thrust penalties negating any ground effect performance improvement.

3) The vortical superstructures generated between rotors with 3.0*R* separation extend higher and over a larger area of the rotor disks than when rotors have 2.5*R* separation.

4) The more widespread turbulence between rotors at 3.0*R* separation intersects with a larger portion of the disk plane, leading to stronger thrust deficits than when rotors are positioned with 2.5*R* separation.

5) The space between rotors at 3.0*R* separation allows for vortical structures to move more freely side-to-side over multiple revolutions. As pockets of strong turbulence move closer to one of the rotors, its thrust average reduces, while the peak-to-peak variation increases significantly (up to 10% of the mean steady thrust).

6) While the more constrained region of turbulence between rotors with 2.5*R* separation does not produce as much rev-to-rev thrust variation as 3*R* separation rotors, more concentrated interrotor vorticity leads to larger 3/rev impulsive loading, with peak-to-peak values increasing as high as 16% of the mean steady thrust.

7) The simulated rotors at H/D = 1 do not observe thrust increment inboard due to fountaining around the hub and through the inboard sections (unlike H/D = 0.5 rotors) and display significantly lower unsteady loading than rotors at H/D = 0.5.

8) The colliding wakes of the two rotors cause the flow to fountain upward as well as to exit the interrotor region laterally (in a direction perpendicular to a plane containing the two rotor hubs).

Appendix

Mesh refinement study

For side-by-side rotors IGE, the region between the rotors where the wakes collide is found to contain highly turbulent flow. This turbulence is encountered by the blades as they pass through the interrotor region inducing impulsive loading. In order to ensure spacial convergence for this important region, a mesh refinement study was performed in which

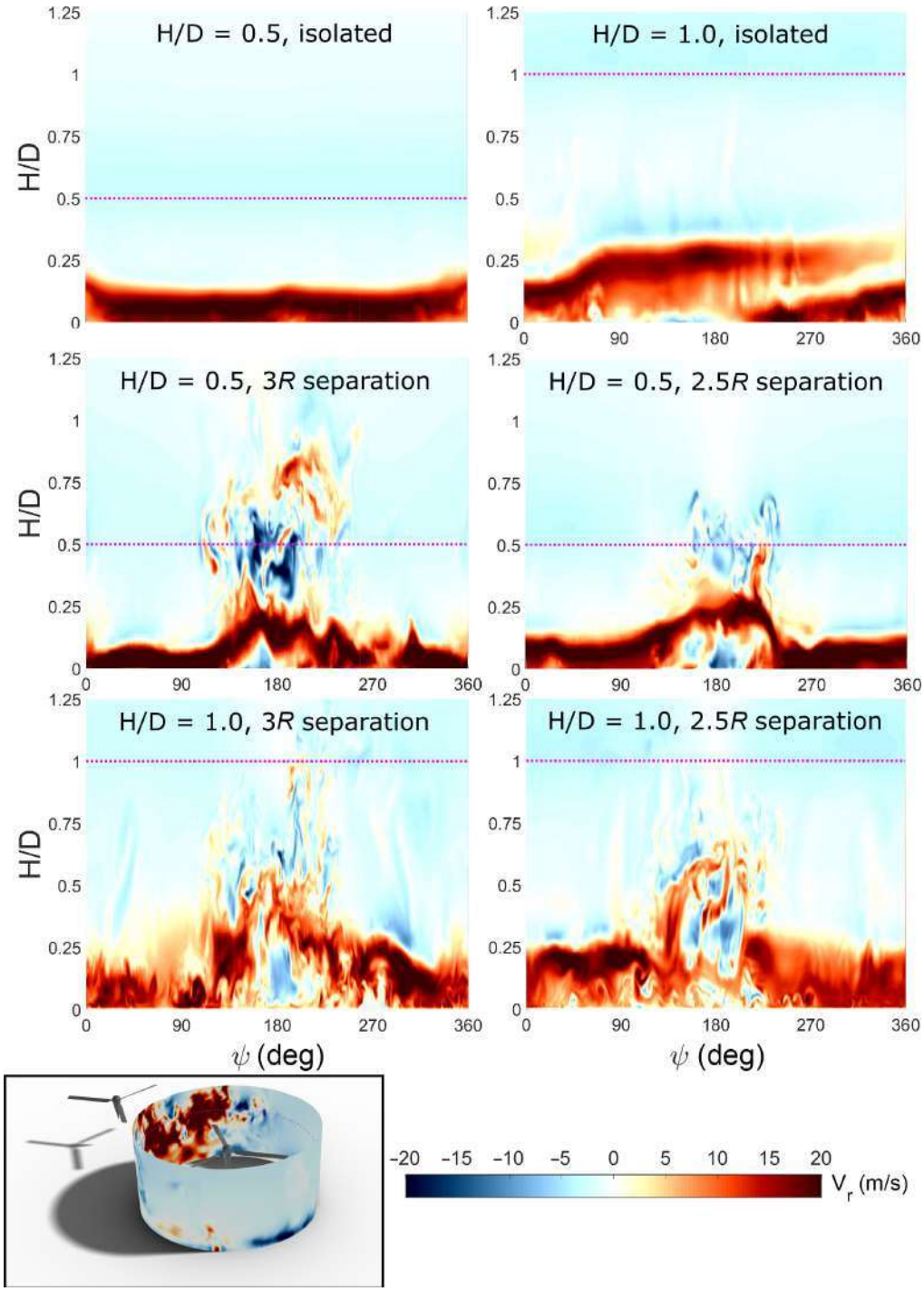

Fig. 25. Unwrapped cylinders colored by radial velocity for IGE rotor cases described in Fig. 1.

the element size in the interrotor region is tested at two levels: 0.25 blade chord (C/4) and 0.125 blade chord (C/8). Side-by-side rotors IGE at H/D = 0.5 with 3.0*R* hub–hub separation (the same as that presented in Fig. 10) are simulated with both levels of refinement and the predicted loads are compared. A slice of each mesh is shown in Fig. A1 with the C/4 refinement mesh containing about 120 million elements and the C/8 refinement mesh containing over 195 million.

While the individual rotor thrust and torque are unsteady with time (as seen in Fig. 13), the both-rotor average is relatively steady and can be compared between cases. Table A1 reports the mean integrated thrust and torque of both rotors averaged over three revolutions. The grid with

Table A1. C/4 and C/8 grid loads

Refinement Level	Thrust	Torque
C/4	642.9 N	60.80 N
C/8	639.1 N	60.20 N
Percent difference	0.6	1.0

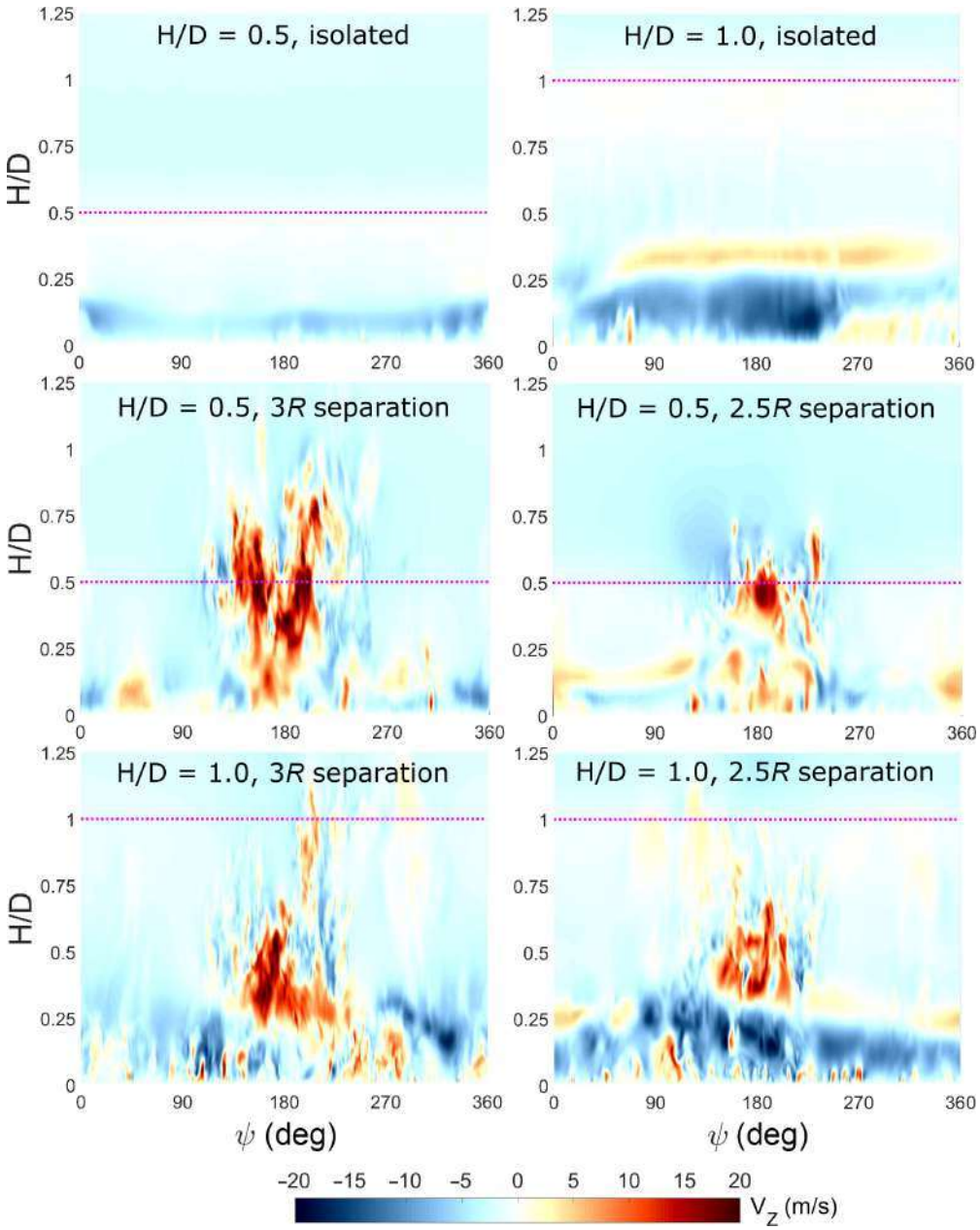

Fig. 26. Unwrapped cylinders colored by vertical velocity for IGE rotor cases described in Fig. 1.

C/4 refinement shows good agreement to the grid with C/8 refinement, with thrust and torque matching to within 1%.

In addition to the average loads, the unsteady loading on the blades is an important aspect to capture. Figure A2 shows the instantaneous and rev-averaged thrust of the left rotor using C/4 and C/8 refinement. Although the stochastic nature of the turbulent mixing region leads to instantaneous thrust differences, the frequency and amplitude of the thrust time histories appear to agree well. Instantaneous thrust ranges from 601.8 to 707.3 N over these revolutions with C/8 refinement, whereas it ranges from 589.1 to 690.9 N with C/4 refinement (a difference of 2.3% and 3.0% between maximum and minimum values, respectively). Rev-averaged loads also compare well, differing by less than 1.5% for 95% of the simulation and showing similar low-frequency phase and amplitude.

In order to better quantify the quality of unsteady loads, a Fourier decomposition of the instantaneous thrust is compared between refinement levels. Figure A3 shows this frequency decomposition of integrated rotor thrust using both refinement levels. When C/8 refinement is used, 15% stronger 3/rev and 22% stronger 6/rev content is observed than when using C/4 refinement, but both capture the peaks at 3, 6, and 9/rev. The low-frequency content at 0.15/rev also compares well between levels, with the amplitude at this frequency lying within 0.25%. Overall, the grid with C/4 refinement captures the harmonic trends of the integrated thrust signal well, and the specific n/rev amplitudes adequately, compared to using a finer grid. Considering the additional computational cost associated with a finer interrotor grid, C/4 is chosen as an acceptable level for identifying the general flow physics and average rotor performance for side-by-side rotors IGE.

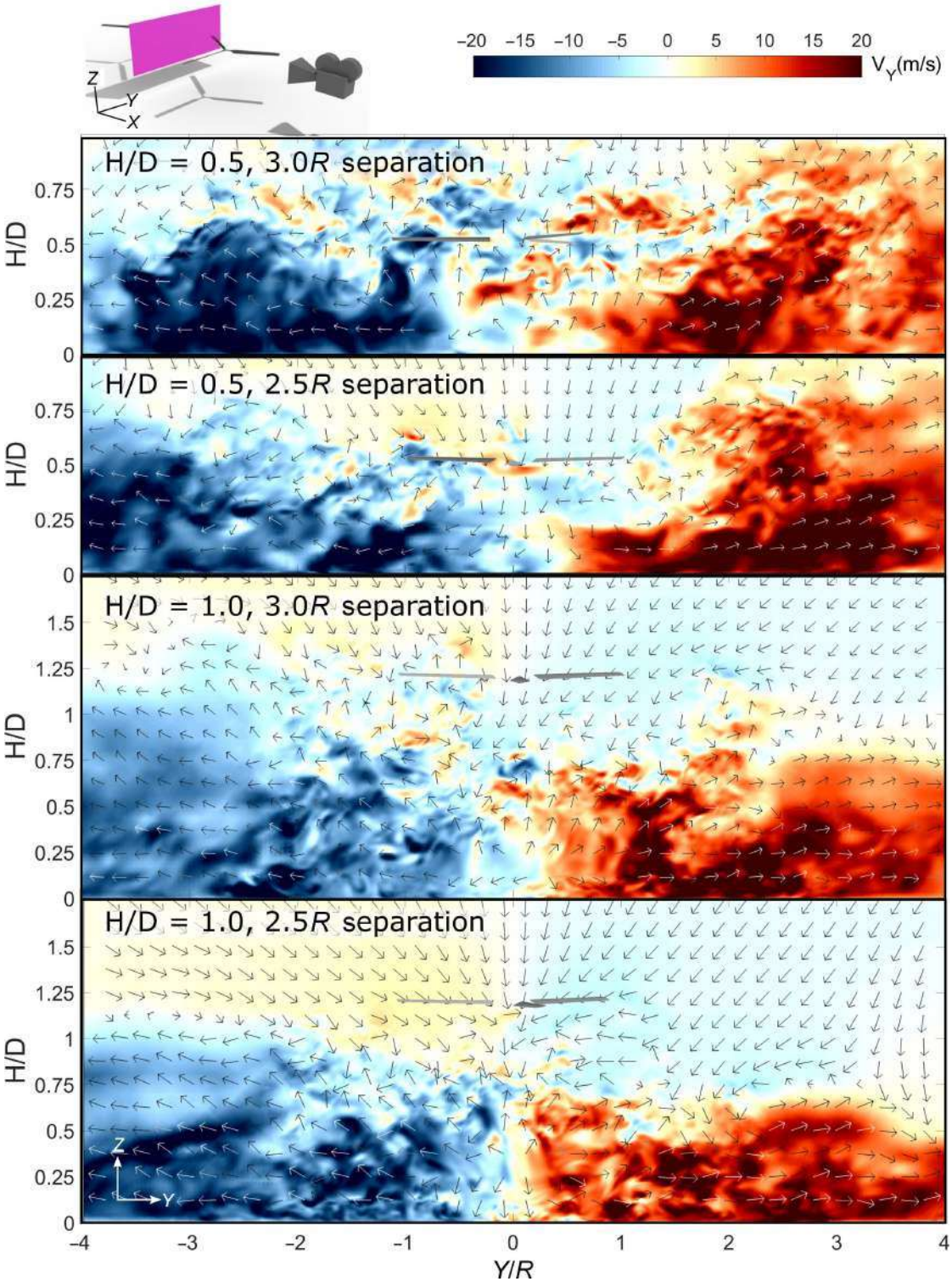

Fig. 27. Slice cutting longitudinally between side-by-side rotors colored by longitudinal velocity.

Temporal refinement study

While time steps corresponding to 1° of rotor rotation per step have been shown to provide good predictions of rotor loads in hover OGE (Ref. [1]), it is necessary to verify that this time step is suitable for side-by-side rotors IGE. In order to test the temporal convergence of IGE rotor simulations, side-by-side rotors at H/D = 0.5 with 3.0*R* hub–hub separation (the same as that presented in Fig. 10) are simulated with time steps corresponding to 1.0° and 0.5° of rotor rotation. In both cases, sufficient subiterations are used to ensure the turbulence and flow residuals converge two orders of magnitude per time step. For most time steps, four stagger iterations are required, regardless of whether time

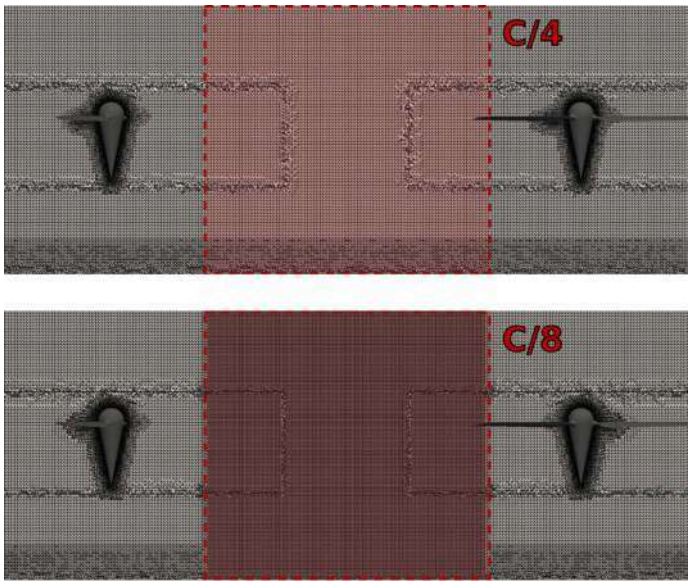

Fig. A1. Crinkle-cut slice through both rotor hubs of meshes with C/4 and C/8 interrotor mesh refinement.

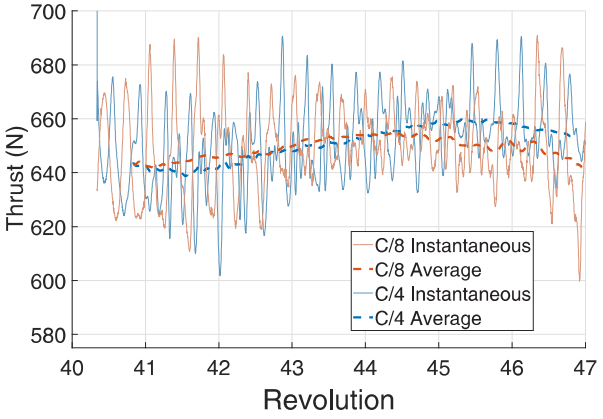

Fig. A2. Left rotor instantaneous and rev-averaged thrust using C/4 and C/8 refinement.

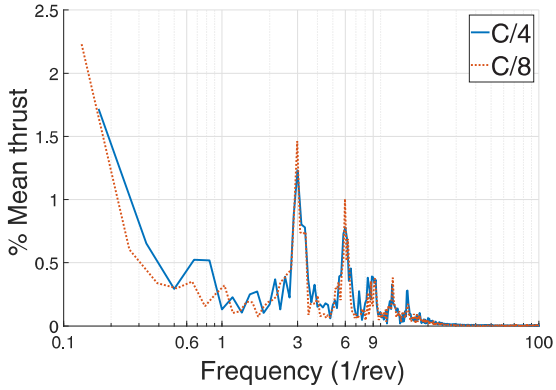

Fig. A3. Frequency decomposition of integrated left rotor thrust using C/4 and C/8 refinement.

Table A2. Loads generated using 1.0° and 0.5° time steps

Time Step	Thrust	Torque
1.0°	648.7 N	60.84 N
0.5°	649.8 N	60.73 N
Percent difference	0.17	0.18

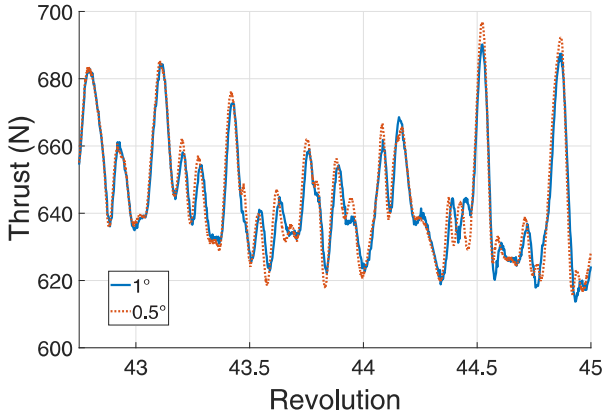

Fig. A4. Left rotor instantaneous and rev-averaged thrust using 1° and 0.5° time steps.

steps correspond to 1.0° or 0.5° of rotor rotation. Table A2 reports the mean integrated thrust and torque of both rotors averaged over three revolutions using each time step.

The predicted thrust and torque using 1° time step compares well to when finer 0.5° time steps are used, with thrust and torque lying within 0.2%. Beyond rev-averaged loads, the unsteady forces generated by the rotor are also of interest. Figure A4 plots the integrated thrust of the left rotor using both 1° and 0.5° time steps. Naturally, some of the high-frequency content is lost when increasing from 0.5° to 1°; however, most of the larger peaks in the loading history loads predicted at 0.5° are also captured at 1°. Not only do the peak–peak amplitudes compare well, but the phase of the signal is also similar between time step levels. These results suggest that 1° time steps provide a sufficient level of temporal convergence that they can capture the same load characteristics as those from a finer time step.

Isolated rotor IGE validation

AcuSolve's® simulation of an isolated rotor IGE is compared to experiment presented in Ref. [10]. A two-bladed rotor with eight root pitch is chosen for comparison. This rotor is simulated at 900 RPM, both IGE at H/D = 1.0 and OGE. This differs somewhat from the setup described in Ref. [10], where IGE rotors spun at 900 RPM are compared to an OGE rotor at 960 RPM. The simulation parameters, including blade mesh resolution, are selected to be similar to those presented with Figs. 2–4. Integrated thrust values predicted by AcuSolve® are found to compare well with experiment, differing by 0.85%. At H/D = 1.0, Ref. [10] reports 33.66 N of thrust while AcuSolve® predicts 33.66 N.

AcuSolve® also predicts thrust for this rotor OGE to be 32.64 N, making $T_{IGE}/T_{OGE} = 1.02$. This is consistent with that reported in Refs. [11] and [56], but slightly less than that reported in Ref. [10] (1.05). Overall, the close agreement with experimental thrust and thrust increment suggests AcuSolve® is capable of accurately predicting ground effect phenomena.

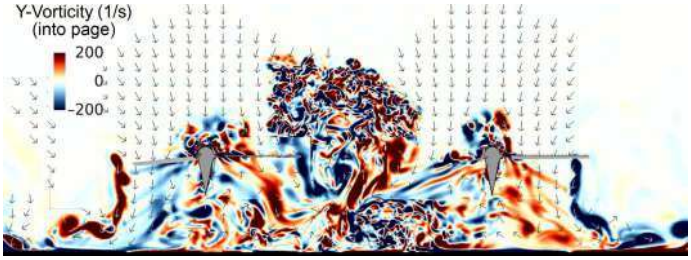

Fig. A5. Slice cutting through side-by-side H/D = 0.5 3.0*R* separation IGE rotor hubs colored by Y-vorticity (simulated with C/8 sized interrotor grid elements).

Flow characteristics with a fine interrotor grid

Figure 12 is recreated in Fig. A5 but using the C/8 interrotor grid case from the mesh refinement study above. Even with the finer grid, the predominant flow characteristics remain similar to those seen in Fig. 12 (which uses a grid with C/4-sized elements between the rotors). On the far left and far right, tip vortices in Fig. A5 convect downwards until they hit the ground and move radially outwards. In the interrotor region, high vorticity flow is observed, with the wakes of each rotor mixing and generating turbulence. This interrotor mixing extends from the ground, up past the rotor disks. For the finer grid case in Fig. A5, the vortices in the interrotor region are naturally finer than those resolved with the coarser grid. The extents of the turbulent flow also reach higher in Fig. A5, extending up to one rotor radius above the disk plane. The interrotor vorticity is also more centered in Fig. A5, not washing over the left rotor to the same degree as that seen in Fig. 12 (though this could be attributed to the stochastic nature of the flow). Overall, the captured flow features remain similar between Figs. 12 and A5, though the finer interrotor grid more intricately resolves smaller-scale vortices and shows the turbulence extending somewhat higher above the rotor disks.

Thrust harmonics for side-by-side rotors IGE

A frequency decomposition of the unsteady loads in Fig. 13 is presented in Fig. A6. Here, the side-by-side rotors at H/D = 0.5 and 3.0*R* hub–hub separation show 3/rev content well in excess of that produced by isolated rotors either IGE or OGE. The 3/rev component for the side-by-side rotors reaches 1.06%, whereas the isolated rotor at H/D = 0.5 only contains 0.15% 3/rev content, and the isolated OGE rotor produces almost none at 0.03%. The 6/rev content for these side-by-side rotors is also relatively high (1.16%), due to the complex aerodynamic environment experienced in the interrotor mixing region. Side-by-side rotors at this height and spacing also show the greatest low-frequency loading associated with the side-to-side movement of the vorticity in the mixing region, as previously discussed. Cycles at 0.17/rev frequency (six revolution period) show amplitudes in excess of 2.2%, further demonstrating the rev-to-rev thrust unsteadiness observed in Fig. 13.

Side-by-side rotors at H/D = 0.5 and 2.5*R* hub–hub separation show the strongest 3/rev content in Fig. A6. As was seen in Fig. 18, the strong 3/rev signal is the result of consistent single impulses as each blade passes through a nonuniform flow field, predominantly in the interrotor mixing region. The more contained mixing region also leads to less low-frequency content, with the 2.5*R* spaced rotors only showing 1.0% amplitude at 0.17/rev (compared to 2.2% amplitude for rotors with 3.0*R* spacing). This is attributed to less side-to-side movement of the vorticity in the mixing region as previously discussed.

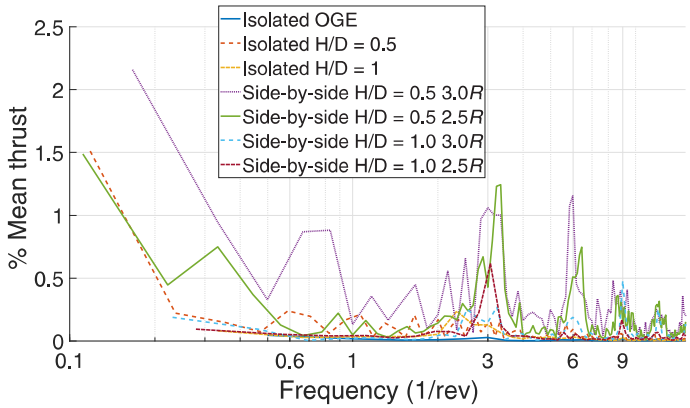

Fig. A6. Frequency decomposition of integrated thrust for the cases presented in Fig. 1.

The relatively low-amplitude unsteady loading seen in Fig. 21 is also manifest in Fig. A6. Whereas side-by-side rotors at H/D = 0.5 produced 3/rev and 6/rev signals in excess of 1%, these rotors at H/D = 1.0 with 3.0*R* spacing only show 0.15% 3/rev and 0.19% 6/rev. Low-frequency amplitudes are also relatively low compared to other cases, further indicating that integrated thrust is relatively steady for these rotors.

The thrust frequency content for rotors at H/D = 1.0 with 2.5*R* spacing shows relatively low amplitude at most frequencies in Fig. A6. However, the 3/rev signal for these rotors is higher than those seen on other rotors at H/D = 1.0 (0.61% at 2.5*R* spacing, 0.15% at 3.0*R* spacing, and 0.13% for an isolated H/D = 1.0 rotor). This trend is similar to that seen on side-by-side rotors at H/D = 0.5 and 2.5*R* spacing, where the closer spacing leads to a more concentrated interrotor mixing region and therefore a strong 3/rev load associated with blade passage. The relatively large 3/rev signal here indicates that even at H/D = 1.0, there is a concentrated interrotor mixing region that induces identifiable impulsive loads for each blade passage.

Acknowledgments

This project was funded by the Boeing Company (Ridley Park, PA) under contract "SSOW-BRT-W0619-5054: Aerodynamic Interaction Study of RPM Controlled Rotors" awarded to Rensselaer Polytechnic Institute's Center for Mobility with Vertical Lift. The support of Dr. Mihir Mistry (Boeing's Program Manager) is gratefully acknowledged.

References

[1]Misiorowski, M., Gandhi, F., and Oberai, A. A., "Computational Study on Rotor Interactional Effects for a Quadcopter in Edgewise Flight," *AIAA Journal*, Vol. 57, (12), 2019, pp. 5309–5319. DOI: 10.2514/1.J058369.

[2]Misiorowski, M., Gandhi, F., and Anusonti-Inthra, P., "Computational Analysis of Rotor-Blown-Wing for Electric Rotorcraft Applications," *AIAA Journal*, Vol. 58, (7), 2020, pp. 2921–2932. DOI: 10.2514/1.J058851.

[3]Healy, R., Misiorowski, M., and Gandhi, F., "A CFD-Based Examination of Rotor-Rotor Separation Effects on Interactional Aerodynamics for eVTOL Aircraft," *Journal of the American Helicopter Society*, **67**, 012006 (2022). DOI: 10.4050/jahs.67.012006.

[4]Healy, R., Gandhi, F., and Mistry, M., "Computational Investigation of Multirotor Interactional Aerodynamics with Hub Lateral and Longitudinal Canting," *AIAA Journal*, Vol. 60, (2), February 2022, pp. 872–882. DOI: 10.2514/1.j060530.

[5]Diaz, P. V., and Yoon, S., "High-Fidelity Computational Aerodynamics of Multi-Rotor Unmanned Aerial Vehicles," Proceedings of the 2018 AIAA Aerospace Sciences Meeting, Kissimmee, FL, January 8–12, 2018.

[6]Yoon, S., Pulliam, T. H., and Chaderjian, N. M., "Simulations of XV-15 Rotor Flows in Hover Using OVERFLOW," AHS 5th Aeromechanics Specialists' Conference, San Francisco, CA, January 22–24, 2014.

[7]Yoon, S., Lee, H. C., and Pulliam, T. H., "Computational Analysis of Multi-Rotor Flows," Proceedings of the 54th AIAA Aerospace Sciences Meeting, San Diego, CA, January 4–8, 2016.

[8]Yoon, S., Diaz, P. V., Boyd, D. D., Jr., Chan, W. M., and Theodore, C. R., "Computational Aerodynamic Modeling of Small Quadcopter Vehicles," Proceedings of the 73rd Annual Forum of the American Helicopter Society, Fort Worth, TX, May 9–11, 2017.

[9]Fradenburgh, E. A., "The Helicopter and the Ground Effect Machine," *Journal of the American Helicopter Society*, Vol. 5, (4), October 1960, pp. 24–33. DOI: 10.4050/jahs.5.4.24.

[10]Hefner, R., and Knight, M., "Analysis of Ground Effect on the Lifting Airscrew," NACA TN, 626, 1945.

[11]Hayden, J. S., "The Effect of the Ground on Helicopter Hovering Power Required," Proceedings of the 32nd Annual Forum of the American Helicopter Society, Washington, DC, May 10–12, 1976.

[12]Light, J. S., "Tip Vortex Geometry of a Hovering Helicopter Rotor in Ground Effect," *Journal of the American helicopter society*, Vol. 38, (2), April 1993, pp. 34–42. DOI: 10.4050/jahs.38.34.

[13]Zbrozek, J., "Ground Effect on the Lifting Rotor," Aeronautical Research Council, 2347, 1947.

[14]Curtiss, H., Sun, M., Putman, W., and Hanker, E., "Rotor Aerodynamics in Ground Effect at Low Advance Ratios," *Journal of the American Helicopter Society*, Vol. 29, (1), 1984, pp. 48–55. DOI: 10.4050/jahs.29.48.

[15]Sheridan, P. F., "Aerodynamics of Helicopter Flight Near the Ground," Proceedings of the 33rd Annual National Forum of the American Helicopter Society, Washington, DC, May American Helicopter Society, 1977.

[16]Nathan, N. D., and Green, R. B., "The Flow around a Model Helicopter Main Rotor in Ground Effect," *Experiments in Fluids*, Vol. 52, (1), October 2011, pp. 151–166. DOI: 10.1007/s00348-011-1212-1.

[17]Bhattacharyya, S., and Conlisk, A., "The Structure of the Rotor Wake in Ground Effect," Proceedings of the 41st AIAA Aerospace Sciences Meeting and Exhibit, January 6–9, 2003.

[18]Griffiths, D. A., Ananthan, S., and Leishman, J. G., "Predictions of Rotor Performance in Ground Effect Using a Free-Vortex Wake Model," *Journal of the American Helicopter Society*, Vol. 50, (4), October 2005, pp. 302–314. DOI: 10.4050/1.3092867.

[19]Moushegian, A. M., Smith, M. J., Whitehouse, G. R., Wachspress, D. A., "Hover Performance in Ground Effect Prediction Using a Dual Solver Computational Methodology," Proceedings of the 77th Annual Forum of the Vertical Flight Society, Virtual, May 10–14, 2021.

[20]Whitehouse, G. R., Wachspress, D. A., and Quackenbush, T. R., "Aerodynamic Design of Helicopter Rotors for Reduced Brownout," International Powered Lift Conference Proceedings, Philadelphia, PA, October 5–7, 2010.

[21]Saberi, H. A., and Maisel, M. D., "A Free-Wake Rotor Analysis Including Ground Effect," Proceedings of the 43rd Annual Forum of the American Helicopter Society, St. Louis, MO, May 18–20, 1987.

[22]Graber, A., Rosen, A., and Seginer, A., "An Investigation of a Hovering Rotor in Ground Effect," *The Aeronautical Journal*, Vol. 95, (945), 1991, pp. 161–169. DOI: 10.1017/S0001924000023812.

[23]Wadcock, A., Ewing, L., Solis, E., Potsdam, M., and Rajagopalan, G., "Rotorcraft Downwash Flow Field Study to Understand the Aerodynamics of Helicopter Brownout," Proceedings of the AHS Southwest Region Technical Specialists' Meeting, October 2008.

[24]Kutz, B., Grossmann, T., Keßler, M., and Krämer, E., "Experimental and Numerical Examination of a Helicopter Hovering in Ground Effect," *CEAS Aeronautical Journal*, Vol. 4, (4), July 2013, pp. 397–408. DOI:10.1007/s13272-013-0084-x.

[25]N. Brooks, A., and Hughes, T. J. R., "Streamline Upwind/Petrov-Galerkin Formulations for Convection Dominated Flows with Particular Emphasis on the Incompressible Navier-Stokes Equations," *Computer Methods in Applied Mechanics and Engineering*, Vol. 32, (1–3), September 1982, pp. 199–259. DOI: 10.1016/0045-7825(82)90071-8.

[26]Lakshminarayan, V. K., Kalra, T. S., and Baeder, J. D., "Detailed Computational Investigation of a Hovering Microscale Rotor in Ground Effect," *AIAA Journal*, Vol. 51, (4), 2013, pp. 893–909. DOI: 10.2514/1.J051789.

[27]Tan, J. F., Sun, Y. M., and Barakos, G. N., "Vortex Approach for Downwash and Outwash of Tandem Rotors in Ground Effect," *Journal of Aircraft*, Vol. 55, (6), November 2018, pp. 2491–2509. DOI: 10.2514/1.c034740.

[28]Ramasamy, M., and Yamauchi, G., "Using Model-Scale Tandem-Rotor Measurements in Ground Effect to Understand Full-Scale CH-47D Outwash," *Journal of the American Helicopter Society*, **62**, (1), 012004 (2017), pp. 1–14. DOI: 10.4050/jahs.62.012004.

[29]Silva, M., and Riser, R., "CH-47D Tandem Rotor Outwash Survey," Proceedings of the 67th Annual Forum of the American Helicopter Society, Virginia Beach, VA, May 3–5, 2011.

[30]Potsdam, M., and Strawn, R., "CFD Simulations of Tiltrotor Configurations in Hover," *Journal of the American Helicopter Society*, Vol. 50, (1), January 2005, pp. 82–94. DOI: 10.4050/1.3092845.

[31]Tran, S., Lim, J., Nunez, G., Wissink, A., and Bowen-Davies, G., "CFD Calculations of the XV-15 Tiltrotor During Transition," Proceedings of the 75th Annual Forum of the American Helicopter Society, Philadelphia, PA, 13–16, 2019.

[32]Polak, D. R., Rehm, W., and George, A. R., "Effects of an Image Plane on the Tiltrotor Fountain Flow," *Journal of the American Helicopter Society*, Vol. 45, (2), April 2000, pp. 90–96. DOI: 10.4050/jahs.45.90.

[33]Rajagopalan, R., "A Procedure for Rotor Performance, Flow field and Interference – A Perspective," Proceedings of the 38th AIAA Aerospace Sciences Meeting and Exhibit, January 10–13, 2000, DOI: 10.2514/6.2000-116.

[34]Gupta, V., and Baeder, J. D., "Quad Tiltrotor Aerodynamics in Ground Effect," Proceedings of the 58th Annual Forum of the American Helicopter Society, Montreal, Canada, June 11–13, 2002.

[35]Radhakrishnan Mylapore, A., and Schmitz, F. H., "An Experimental Investigation of Ground Effect on a Quad Tilt Rotor in Hover," *Journal of the American Helicopter Society*, **60**, 012002 (2015), DOI: 10.4050/jahs.60.012002.

[36]Radhakrishnan, A., and Schmitz, F., "An Experimental Investigation of a Quad Tilt Rotor in Ground Effect," Proceedings of the 21st AIAA Applied Aerodynamics Conference, June 23–26, 2003, DOI: 10.2514/6.2003-3517.

[37]Radhakrishnan, A., and Schmitz, F., "Quad Tilt Rotor Aerodynamics in Ground Effect," Proceedings of the 23rd AIAA Applied Aerodynamics Conference, June 6–9, 2005, DOI: 10.2514/6.2005-5218.

[38]Radhakrishnan, A., and Schmitz, F., "Aerodynamics and Lifting Performance of a Quad Tilt Rotor in Ground Effect," Paper 292, Proceedings of the 63rd Annual Forum of the American Helicopter Society, Virginia Beach, VA, May 1–3, 2007.

[39]Miesner, S., Keßler, M., Krämer, E., and Schäferlein, U., "Investigation of Near Ground Effects in Hover Flight for the Multi-Rotor Aircraft Volocopter-2X," Paper 16409, Proceedings of the 76th Annual Forum of the Vertical Flight Society, Virtual, October 5–8, 2020.

[40]Hariharan, N. S., Narducci, R. P., Reed, E., and Egolf, A., "AIAA Standardized Hover Simulation: Hover Performance Prediction Status and Outstanding Issues," Proceedings of the 55th AIAA Aerospace Sciences Meeting, Grapevine, TX, January 9–13, 2017.

[41]Abras, J., Narducci, R. P., and Hariharan, N. S., "Impact of High-fidelity Simulation Variations on Wake Breakdown of a Rotor in Hover," Proceedings of the AIAA SciTech 2020 Forum, Orlando, FL, January 6–10, 2020. DOI: 10.2514/6.2020-0531.

[42]Niemiec, R., and Gandhi, F., "Development and Validation of the Rensselaer Multicopter Analysis Code (RMAC): A Physics-based Low-fidelity Modeling Tool," Paper 367, Proceedings of the 75th Annual Forum of the Vertical Flight Society, Philadelphia, PA, May 13–16, 2019.

[43]ACUSIM Software, Inc., "AcuSolve Validation - NACA 0012 Airfoil," AcuSolve Validation Manual, available at https://2021.help.altair.com/2021/hwsolvers/acusolve/topics/acusolve/turbulent_flow_over_a_naca_airfoil.htm, accessed date April 1, 1923.

[44]Corson, D., Jaiman, R., and Shakib, F., "Industrial Application of RANS Modelling: Capabilities and Needs," *International Journal of Computational Fluid Dynamics*, Vol. 23, (4), 2009, pp. 337–347. DOI: 10.1080/10618560902776810.

[45]Misiorowski M., "Understanding and Improvement of eVTOL UAV Performance through High-Fidelity Analysis of Interactional Aerodynamics," Ph.D. thesis, Rensselaer Polytechnic Institute, August 2019.

[46]ACUSIM Software, Inc., A. E., "Modeling of Turbulence - Near-Wall Modeling," AcuSolve Training Manual, https://2021.help.altair.com/2021/hwsolvers/acusolve/topics/acusolve/training_manual/near_wall_modeling_r.htm#reference_njv_q5k_2w, accessed date April 1, 2023.

[47]Bazilevs, Y., Michler, C., Calo, V., and Hughes, T., "Weak Dirichlet Boundary Conditions for Wall-bounded Turbulent Flows," *Computer Methods in Applied Mechanics and Engineering*, Vol. 196, (49), 2007, pp. 4853–4862. DOI: https://doi.org/10.1016/j.cma.2007.06.026.

[48]Boisard, R., "Aerodynamic Investigation of a Helicopter Rotor Hovering in the Vicinity of a Building," Paper 61, Proceedings of the 74th Annual Forum of the American Helicopter Society, Phoenix, AZ, May 14–17, 2018.

[49]Karthikeyan Duraisamy, K., and Baeder, J. D., "High Resolution Wake Capturing Methodology for Hovering Rotors," *Journal of the American Helicopter Society*, Vol. 52, (2), April 2007, pp. 110–122, DOI: 10.4050/jahs.52.110.

[50]Richez, F., and Ortun, B., "Numerical Investigation of the Flow Separation on a Helicopter Rotor in Dynamic Stall Configuration," Proceedings of the 42nd European Rotorcraft Forum, Lille, France, November 6–8, 2017.

[51]Jain, R. K., Lim, J. W., and Jayaraman, B., "Modular Multisolver Approach for Efficient High-Fidelity Simulation of the HART II Rotor," *Journal of the American Helicopter Society*, **60**, 032001 (2015), DOI: 10.4050/jahs.60.032001.

[52]Jansen, K. E., Whiting, C. H., and Hulbert, G. M., "A Generalized-α Method for Integrating the Filtered Navier–Stokes Equations With a Stabilized Finite Element Method," *Computer Methods in Applied Mechanics and Engineering*, Vol. 190, (3), 2000, pp. 305–319. DOI: https://doi.org/10.1016/S0045-7825(00)00203-6.

[53]Cheeseman, I., and Bennett, W., "The Effect of the Ground on a Helicopter Rotor in Forward Flight," ARC R&M, 3021, September 1955.

[54]Brown, R. E., and Whitehouse, G. R., "Modelling Rotor Wakes in Ground Effect," *Journal of the American Helicopter Society*, Vol. 49, (3), July 2004, pp. 238–249. DOI: 10.4050/jahs.49.238

[55]Zhou, W., Ning, Z., Li, H., and Hu H., "An Experimental Investigation on Rotor-to-Rotor Interactions of Small UAV Propellers," Proceedings of the 35th AIAA Applied Aerodynamics Conference, Denver, CO, June 5–9, 2017, DOI: 10.2514/6.2017-3744.

[56]Fradenburgh, E. A., "Aerodynamic Factors Influencing Overall Hover Performance," *AGARD Conference Proceedings No. 111*, Advisory Group for Aerospace Research and Development, Marseilles, France, 1972.